

## RESEARCH ARTICLE

## Fracture toughness anisotropy in shale

10.1002/2015JB012756

## Key Points:

- Mancos shale displays mechanical anisotropy in terms of tensile strength and fracture toughness
- Ductility for Mancos shale is high, but not significantly higher than for other sedimentary rocks
- Fractures are commonly seen to deflect into the Short Transverse orientation during experiments

## Correspondence to:

M. R. Chandler,  
mike.chandler@manchester.ac.uk

## Citation:

Chandler, M. R., P. G. Meredith, N. Brantut, and B. R. Crawford (2016), Fracture toughness anisotropy in shale, *J. Geophys. Res. Solid Earth*, 121, 1706–1729, doi:10.1002/2015JB012756.

Received 17 DEC 2015

Accepted 4 MAR 2016

Accepted article online 9 MAR 2016

Published online 31 MAR 2016

Michael R. Chandler<sup>1,2</sup>, Philip G. Meredith<sup>1</sup>, Nicolas Brantut<sup>1</sup>, and Brian R. Crawford<sup>3</sup>

<sup>1</sup>Rock and Ice Physics Laboratory, Department of Earth Sciences, University College London, London, UK, <sup>2</sup>Now at School of Earth, Atmospheric and Environmental Sciences, University of Manchester, Manchester, UK, <sup>3</sup>ExxonMobil URC, Houston, Texas, USA

**Abstract** The use of hydraulic fracturing to recover shale gas has focused attention on the fundamental fracture properties of gas-bearing shales, but there remains a paucity of available experimental data on their mechanical and physical properties. Such shales are strongly anisotropic, so that their fracture propagation trajectories depend on the interaction between their anisotropic mechanical properties and the anisotropic in situ stress field in the shallow crust. Here we report fracture toughness measurements on Mancos shale determined in all three principal fracture orientations: Divider, Short Transverse, and Arrester, using a modified short-rod methodology. Experimental results for a range of other sedimentary and carbonate rocks are also reported for comparison purposes. Significant anisotropy is observed in shale fracture toughness measurements at ambient conditions, with values, as high as 0.72 MPa m<sup>1/2</sup> where the crack plane is normal to the bedding, and values as low as 0.21 MPa m<sup>1/2</sup> where the crack plane is parallel to the bedding. For cracks propagating nonparallel to bedding, we observe a tendency for deviation toward the bedding-parallel orientation. Applying a maximum energy release rate criterion, we determined the conditions under which such deviations are more or less likely to occur under more generalized mixed-mode loading conditions. We find for Mancos shale that the fracture should deviate toward the plane with lowest toughness regardless of the loading conditions.

## 1. Introduction

Shales are commonly deposited in deep marine environments, covering very broad areas [Burns, 2011]. As a result, they are the most abundant of sedimentary rock types, making up 50–80% of sedimentary material worldwide. Their mechanical properties are therefore of great interest as both source and caprocks for hydrocarbon resources. Over the last decade hydraulic fracturing of gas shales has led to renewed interest in their mechanical and microstructural properties. The propagation of hydraulic fractures is dependent on a combination of the in situ stress field, the pore pressure, fracturing fluid pressure, and the mechanical properties of the rock [Warpinski and Smith, 1990].

Fracture toughness is an important mechanical property influencing hydraulic fracture propagation, particularly so in cases where the stress contrasts are small, the fluid is of low viscosity, and the fracture is relatively small [Thiercelin *et al.*, 1989]. Both the magnitude and anisotropy of crustal stress increase with increasing depth; hence, the influence of fracture toughness and its anisotropy on fracture propagation is maximum at shallow depths, where it is possible for large horizontal fractures to be generated [Eseme *et al.*, 2007; Khazan and Fialko, 1995].

Despite this importance, fracture toughness data on shales are very sparse. The microstructure of shales makes material recovery, preservation, and sample manufacture very difficult and also militates against performing consistent and reproducible experiments. Only three published studies consider measurements in more than one orientation. Schmidt and Huddle [1977a] used three-point bend specimens to measure mode-I fracture toughness,  $K_{Ic}$  values varying from 0.3 to 1.1 MPa m<sup>1/2</sup> for two grades of Anvil Points oil shale in three orthogonal orientations. They found that increased hydrocarbon content produced lower fracture toughness values and that in both cases cracks oriented normal to bedding produced the highest values, while cracks oriented parallel to bedding produced the lowest values. Lee *et al.* [2015] used semicircular bend specimens to measure  $K_{Ic}$  values varying from 0.18 to 0.73 MPa m<sup>1/2</sup> for Marcellus shale samples along two orthogonal directions normal to bedding and for fractures propagating at 60° to the bedding plane. They report that the bedding normal fractures produced the highest and the 60° inclined fractures the lowest  $K_{Ic}$  value.

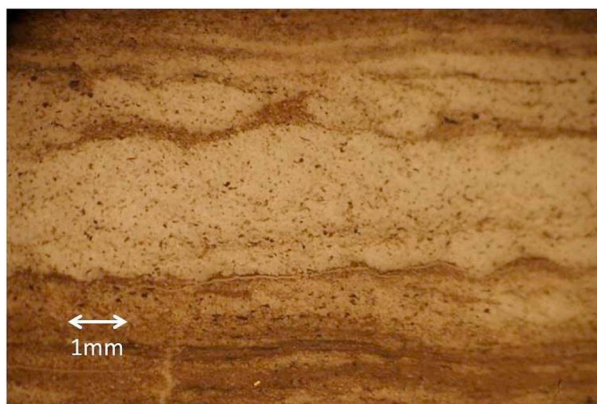


**Figure 1.** Optical microscope image of layering in Mancos shale. Interbedded layers of (dark) fine grained clay material and (light) coarser layers of siltstone material are seen and observed to undulate substantially. Figure courtesy of (J. Ahmed, personal communication, 2014).

*Chong et al.* [1987] provide a summary of their own results, together with those of *Costin* [1981] and *Young et al.* [1982] on oil shales for bedding normal fractures propagating parallel to bedding, finding  $K_{Ic}$  to vary over the range 0.6–1.1 MPa m<sup>1/2</sup>, but demonstrating the opposite trend from *Schmidt and Huddle* [1977a], with both fracture toughness and ductility increasing with increasing hydrocarbon content. *Warpinski and Smith* [1990] quote a fracture toughness value of 1.43 MPa m<sup>1/2</sup> for the Mancos shale but do not provide information about the methodology or fracture orientation.

Here we report results from a systematic suite of characterization and fracture toughness measurements on samples of Mancos shale under ambient conditions, as well as measurements of fracture toughness on a range of other sedimentary and carbonate rock materials for purposes of comparison: Carrara marble, Darley Dale sandstone, Clashach sandstone, Crab Orchard (Tennessee) sandstone, Portland limestone, Sölnhofen limestone, and Indiana limestone. Specifically, the density, porosity, ultrasonic wave velocities, tensile strength, and fracture toughness have been measured on samples of Mancos shale under ambient conditions. We then use a fracture propagation criterion based on the maximum energy release rate [*Nuismer*, 1975] with our anisotropic fracture toughness measurements to make predictions about fracture deviations between different orientations with respect to bedding.

## 2. Characterization of the Mancos Shale

### 2.1. Petrological Properties

The Mancos shale is an Upper Cretaceous shale deposited 90–70 Ma in the Rocky Mountain area of western Colorado and eastern Utah and provides the source for many of the shale plays in the Rockies [*Longman and Koepsell*, 2005]. The Mancos is an unusually thick formation (up to 1100 m) of various shale lithotypes including interbedded claystone, siltstone, and very fine grained sandstone [*Chidsey and Morgan*, 2010]. Organic content and maturity are generally quite low, but there are several kerogen-rich members, and gas shows throughout [*Schamel*, 2005].

Figures 1 and 2 show a photograph and a magnified scanning electron microscope (SEM) image of the layered structure of Mancos shale, respectively. The layering within the material is visible from the micrometer to the centimeter scale.

A petrographical assessment of eight thin sections of our Mancos shale material was conducted using both optical and scanning electron microscope (SEM) microscopy by *King* [2013]. The fine-grained nature of the shale material means that it is not possible to identify many features at optical resolution. Each section was seen to be made up of laminations of alternating light grey and brown layers. This layering varies from submillimeter to centimeters in thickness. The brown layers comprise fine-grained clay matrix, containing elongate fragments of organic matter. The light grey layers comprise terrigenous sand and silt, containing light grey calcite cement. Occasional quartz grains are present within both the clay and silt layers, although they occur in greater concentrations within the silt layers. These quartz grains exhibit no preferred orientation but display undulose extinction under optical microscopy. Anhedral plagioclase grains were also present, again without

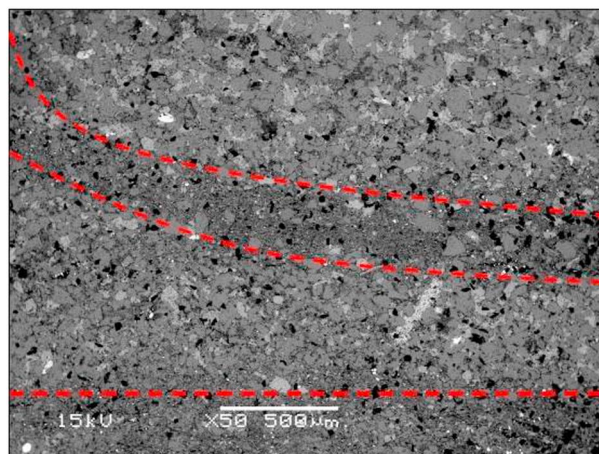


**Figure 2.** SEM image showing layering within the Mancos shale. Narrow layers of fine-grained clay material (dark) are interwoven with bands of silt material (light) containing calcite, dolomite, feldspar, and quartz grains. Black spots of organic material are visible within both layer types. Figure modified after King [2013].

any specific alignment. Additionally, grains of euhedral dolomite and calcite are present, suggesting that diagenetic processes have occurred. The thinly laminated structure is shown in Figure 2 and is as expected for these outcrop samples as it suggests that they are not deep sourced [Loucks *et al.*, 2012]. McLennan *et al.* [1983] used X-ray diffraction analysis to study samples of Mancos shale and found a content of 25–100% quartz, 10–30% dolomite, with components less than 15% of calcite, illite, kaolinite, chlorite, feldspar, pyrite, and apatite. These components agree broadly with the mineralogical interpretation of SEM elemental analysis on our material conducted by King [2013].

### 2.2. Physical Properties

We measured both density and porosity on cores of Mancos shale. Connected porosity and total porosity were both measured using the Helium pycnometer in the Fragmentation Laboratory at LMU Munich before and after crushing of the sample, respectively. The connected porosity value was confirmed from measurements at UCL using the triple weight method with decane as the pore fluid, following Sarker and Batzle [2010]. The measured values are presented in Table 1, together with values from Terratek [2008], Kennedy [2011], and Sarker and Batzle [2010]. The data of Sarker and Batzle [2010] were measured on the Mancos B subunit of the Mancos shale.

### 2.3. Elastic Properties

Ultrasonic wave velocities were characterized at ambient conditions using the pulse-transmission method described by Benson *et al.* [2003] with 1 MHz transducers. Due to the clear layered nature of Mancos shale seen in the images of Figures 1 and 2, the wave velocity was treated as anisotropic and measured over a

**Table 1.** Summary of Physical and Mechanical Properties of the Mancos Shale Reported by Terratek [2008], Kennedy [2011], Sarker and Batzle [2010], and This Study<sup>a</sup>

Property	Terratek [2008]	Kennedy [2011]	Sarker and Batzle [2010]	This Study
Bulk density (kg m <sup>-3</sup> )	2540			2630 ± 300
Uniaxial compressive strength (MPa)	68	97.8 ± 18.4		67
Total porosity (%)				9.24 ± 0.75
Open porosity (%)	7.9	5.55 ± 1.35	6.6	4.18 ± 1.72
Permeability (nD)	< 1	0.16 ± 0.05	0.008–0.2	
Young's modulus (GPa)		23.528 ± 2.668		24.80
Poisson's ratio		0.183 ± 0.0183		0.08–0.23
Mineralogy			39% Quartz, 33% Clay Minerals, 17% Carbonates	10–25% Quartz, 5% Dolomite, 5% Feldspar, 1–2% Calcite

<sup>a</sup>The Young's modulus and Poisson's ratio from this study was determined during the bedding-parallel compressive strength experiment described in section 2.4.

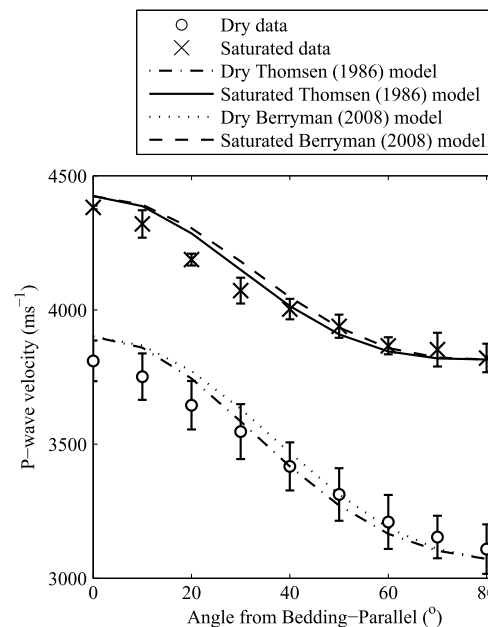


**Figure 3.** Variation of ultrasonic  $P$  wave velocity with angle from bedding parallel, using the transverse isotropy of the shale to convert the data into a  $90^\circ$  angle range. The velocity through the saturated material is  $\approx 600 \text{ m s}^{-1}$  faster than through the dry material, but the difference increases when perpendicular to the bedding. This suggests that the material contains cracks aligned parallel to the bedding plane. Waves traveling perpendicular to the cracks are more affected by the change in seismic velocity of the saturating fluid. The *Thomsen* [1986] and *Berryman* [2008] fits are seen to be very similar.

range of orientations. Specifically,  $P$  wave and  $S$  wave travel time measurements were taken at increments of  $10^\circ$  around the azimuth of 38.1 mm diameter samples cored both parallel and normal to bedding. At each azimuth 4096 received waveforms were stacked, in order to improve the signal-to-noise ratio.  $P$  wave velocity ( $v_p$ ) measurements were made on both dry and saturated samples, with decane used as the saturating fluid to avoid any problems associated with swelling of the clay particles in the presence of water (again, following *Sarker and Batzle* [2010]). Horizontally polarized  $S$  wave velocity ( $v_{sH}$ ) measurements were made only on dry samples.

The velocity data measured as a function of azimuth around samples cored parallel to the bedding are presented in Figures 3 and 4. The velocity data measured as a function of azimuth within the bedding plane (i.e., on dry samples cored perpendicular to bedding) showed no significant variation and were all within the experimental error at  $v_p = 3810 \pm 76 \text{ m s}^{-1}$  and  $v_s = 2350 \pm 36 \text{ m s}^{-1}$ .

Figure 3 shows that  $v_p$  exhibits significant anisotropy for azimuths nonparallel to bedding. The dry value of  $v_p$  normal to bedding is  $750 \text{ m s}^{-1}$  slower than the bedding-parallel value of  $3800 \text{ m s}^{-1}$ . The introduction of decane as a saturating fluid increased  $v_p$  by  $570 \text{ m s}^{-1}$  in the bedding parallel direction and  $750 \text{ m s}^{-1}$  in the bedding normal direction.

Figure 4 shows similarly that  $v_{sH}$  exhibits an anisotropy for azimuths nonparallel to bedding, with the bedding normal value being  $255 \text{ m s}^{-1}$  slower than the bedding-parallel value of  $2350 \text{ m s}^{-1}$ . Overall, the data indicate transversely isotropic behavior, consistent with our qualitative macrostructural and microstructural observations (Figures 1 and 2).

The velocity anisotropy parameters of *Thomsen* [1986] and *Berryman* [2008] were subsequently derived from the azimuthal measurements and are presented in Table 2 and illustrated in Figures 3 and 4. The two fits are seen to be rather similar and match the data within 2%. The weak  $P$  wave elastic anisotropy parameter,  $\epsilon$ , was calculated according to the methodology of *Thomsen* [1986].  $\epsilon_{\text{dry}}$  was found to be 24%, while  $\epsilon_{\text{sat}}$  was found to be 17%, which is significantly higher than the 9% reported by *Sarker and Batzle* [2010]. These  $\epsilon$  values are at the high end of the range of shale anisotropy values given by *Thomsen* [1986].

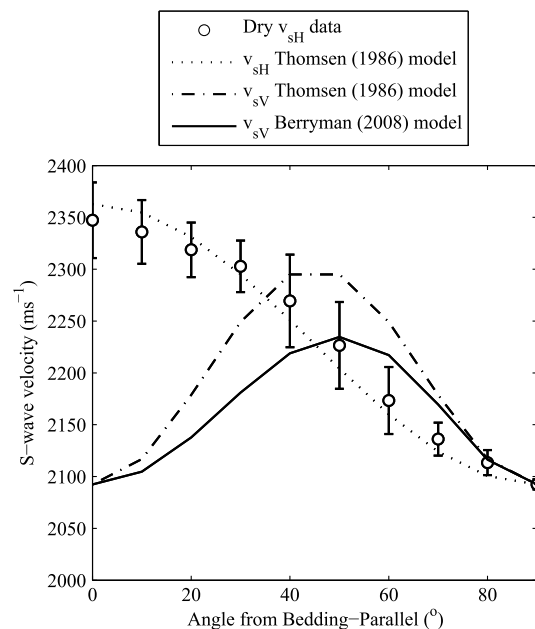


**Figure 4.** Variation of ultrasonic SH wave velocity in dry Mancos shale with angle from bedding perpendicular, using the transverse isotropy of the shale to convert the data into a 90° angle range. Also plotted are the *Thomsen* [1986] and *Berryman* [2008] models of SV wave velocity in dry Mancos shale. The models of *Thomsen*, and *Berryman*, predict identical functions for  $v_{sH}$ .

The substantial decrease in  $\epsilon$  between dry and decane saturated samples suggests that at least some of the  $P$  wave anisotropy is caused by microcracks-aligned parallel to the bedding planes. The change in the seismic velocity due to the change in fluid content affects waves traveling perpendicular to the cracks more than it does waves traveling parallel to the cracks [Pyrak-Nolte et al., 1990]. Therefore, a decrease in anisotropy with fluid saturation suggests that microcracks within the material are preferentially oriented parallel to the bedding planes.

The  $v_{sH}$  anisotropy,  $\gamma$  [Thomsen, 1986], was found to be 13%. This  $\gamma$  value is at the very low end of the range found for gas shale materials by Sone and Zoback [2013], and the low end of the wide range of 2 to 55% reported for a variety of shale materials by Wang [2002a]. However, it is higher than the  $S$  wave anisotropy value of 5% reported by Sarker and Batzle [2010] for saturated Mancos B shale samples.

Finally, we derived dynamic elastic moduli from our velocity measurements and the density value from Table 1, using the method described by Wang [2002b]. These results are summarized in Table 3.

**Table 2.** Anisotropy Properties of *Thomsen* [1986], *Berryman*[2008], and *Tsvankin* [2001] for the Dry and Saturated Mancos Shale<sup>a</sup>

Anisotropy Parameter	Dry Mancos Shale	Saturated Mancos Shale
$\epsilon$	27%	16%
$\gamma$	13%	-
$\delta$	9%	-1%
$v_p(0)(m s^{-1})$	$3063 \pm 117$	$3816 \pm 74$
$v_s(0)(m s^{-1})$	$2092 \pm 5$	-
$\zeta_m$	34%	34%
$\theta_m$	35°	40°
$\eta$	13%	16%

<sup>a</sup> $\epsilon$  and  $\gamma$  are the  $P$  wave and  $S$  wave anisotropies, respectively.  $\delta$  is a measure of the wavefront ellipticity.  $v_p(0)$  and  $v_s(0)$  are the bedding-perpendicular  $P$  and  $S$  wave velocities, respectively.  $\zeta_m$  and  $\theta_m$  are additional parameters used in the method of *Berryman* [2008].  $\eta$  is the anellipticity parameter of *Tsvankin* [2001].

**Table 3.** Dynamic Elastic Constants of the Mancos Shale, Calculated From the Ultrasonic Velocities Using the Methods of Wang [2002b]

Material	$c_{11}$ (GPa)	$c_{66}$ (GPa)	$c_{44}$ (GPa)	$c_{33}$ (GPa)	$c_{13}$ (GPa)	$c_{12}$ (GPa)
Dry Mancos Shale	38.2	14.5	11.5	24.7	3.7	9.2
Decane-Saturated Mancos Shale	50.5	14.5	11.5	38.3	14.8	21.5

### 2.4. Strength

Our macrostructural and microstructural observations and our measurements of wave velocity anisotropy all indicate that Mancos shale exhibits transverse isotropy. We would therefore also expect to observe similar anisotropy in its mechanical properties.

In transversely isotropic media, we can define three principal crack orientations with respect to the isotropy (bedding) plane, as described by Schmidt and Huddle [1977a] and Chong et al. [1987]. The principal orientations are known as Divider, Short Transverse, and Arrester, respectively, and are illustrated in Figure 5.

In the Divider orientation, the crack plane is normal to the isotropy (bedding) plane, but the crack propagates in a direction parallel to the isotropy plane. In the Short Transverse orientation both the crack plane and the crack propagation direction are parallel to the isotropy plane. Finally, in the Arrester orientation, both the crack plane and the crack propagation direction are normal to the isotropy plane. For a horizontally bedded material like Mancos shale, the Divider, Short Transverse, and Arrester orientations correspond respectively to a vertically oriented fracture propagating horizontally, a horizontal fracture propagating horizontally, and a vertically propagating fracture.

We therefore determined the tensile strength of dry samples of Mancos shale in each of the three principal orientations using the Brazilian Disk technique described by International Society of Rock Mechanics (ISRM) [1978]. A vertical compressive load was applied across the 38.1 mm diameter of 19 mm thick rock disks, at a strain rate of  $4 \times 10^{-5} \text{ s}^{-1}$ . The tensile strength,  $\sigma_T$ , was then determined directly from the maximum applied load,  $P_{\text{max}}$  and the sample dimensions, according to

$$\sigma_T = 0.636 \frac{P_{\text{max}}}{Dt} \tag{1}$$

where  $P$  is the failure load,  $D$  is the sample diameter, and  $t$  is the sample thickness [ISRM, 1978].

Table 4 lists the mean tensile strengths and their standard deviations for each orientation. As expected, significant strength anisotropy is observed. Our Divider orientation  $\sigma_T$  values have a mean value of  $5.8 \pm 0.6$  MPa with a standard deviation of around 10% and lie within the range of  $6.4 \pm 2.3$  MPa for a range of Mancos shale samples reported by Kennedy [2011]. In the Short Transverse orientation we observe two distinct clusters of  $\sigma_T$  values labeled as low and high. There is very little scatter within each cluster of measurements (standard deviations of 4% and 3%, respectively). We therefore interpret this as a bimodal  $\sigma_T$  distribution rather than a large scatter on a single  $\sigma_T$  value. The lower value of  $4.54 \pm 0.16$  MPa is the lowest  $\sigma_T$  recorded for any orientation. By contrast, the higher value of  $7.35 \pm 0.22$  MPa is the highest tensile strength recorded for any orientation.

Finally,  $\sigma_T$  in the Arrester orientation was  $7.3 \pm 1.3$  MPa, but measurements in this orientation exhibited the highest scatter, with a standard deviation of 18%. In addition, results from approximately half of the Arrester orientation tests had to be discarded because the fracture deviated significantly from the diametral plane toward the Short Transverse orientation, resulting in erroneous and anomalously low apparent tensile strengths. An example of a sample from a discarded test is shown in Figure 6. The deviation of fractures away

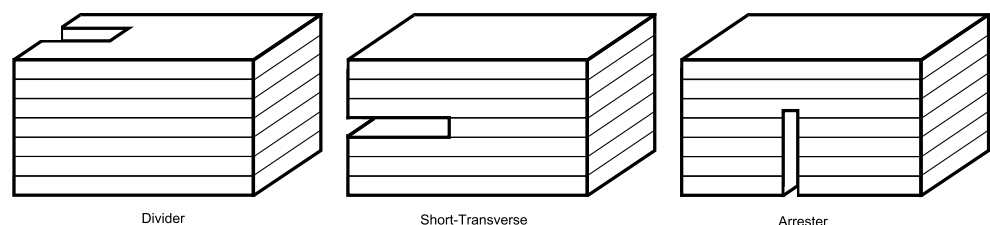


**Figure 5.** The three principal crack-plane orientations relative to bedding (anisotropy) planes: Divider, Short Transverse, and Arrester. Figure modified after Chong et al. [1987].

**Table 4.** Tensile Strength Values of the Mancos Shale Measured Across the Three Principal Crack Orientations Described in Section 2.4

Crack Orientation	$\sigma_T$ (MPa)	$n_{\text{repeats}}$
Divider	$5.81 \pm 0.57$	4
Short transverse <sub>low</sub>	$4.54 \pm 0.16$	4
Short transverse <sub>high</sub>	$7.35 \pm 0.22$	3
Arrester	$7.28 \pm 1.29$	7

from the principal plane in Arrester orientation tests was a significant issue throughout this study and is discussed in detail later. Our tensile strength value for the Arrester orientation agrees reasonably well with that of  $6.38 \pm 2.32$  MPa, for borehole samples using the same methodology, published by Kennedy [2011].

We also attempted to determine the unconfined compressive strength (UCS) of Mancos shale parallel and normal to bedding using the *American Society for Testing and Materials* [2002] recommended methodology which makes use of cylindrical samples with a 3:1 length:diameter ratio. We were able to measure UCS on a single sample cored parallel to bedding but were unable to produce any cores normal to bedding with the required aspect ratio. All bedding normal cores were found to disk off during coring before reaching the required length. Our single (dry) bedding parallel UCS measurement of 67 MPa is given in Table 1. It agrees closely with the value of 68 MPa reported by Terratek [2008] but is substantially lower than the value reported by Kennedy [2011] in the bedding parallel orientation.

### 3. Experimental Fracture Toughness Methodology

Fracture toughness measurements on dry Mancos shale and all the comparator materials were made using the short-rod methodology suggested by *ISRM* [1988] and variants thereof (detailed below). Cylindrical specimens with a 60 mm diameter were used here, and this technique involves a chevron-notch cut parallel to the cylindrical axis to leave a triangular ligament of intact material. In the standard [*ISRM*, 1988] sample, a broad, shallow groove is also machined into the top surface of the sample, parallel to the chevron notch, to allow the sample to be loaded.

A tensile load is then applied within the groove, in a direction normal to the triangular ligament perpendicular to the plane of the chevron, as shown in Figure 8 (right-hand side). The tensile load causes a crack to nucleate

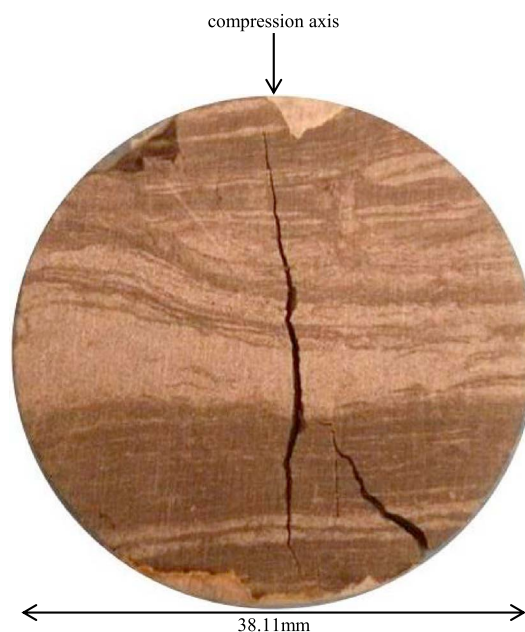


**Figure 6.** An example of an Arrester-orientation Brazilian Disk test which has suffered deviated fracture. The anisotropy in the material strength leads to the fracture deflecting toward the weaker Short Transverse orientation.

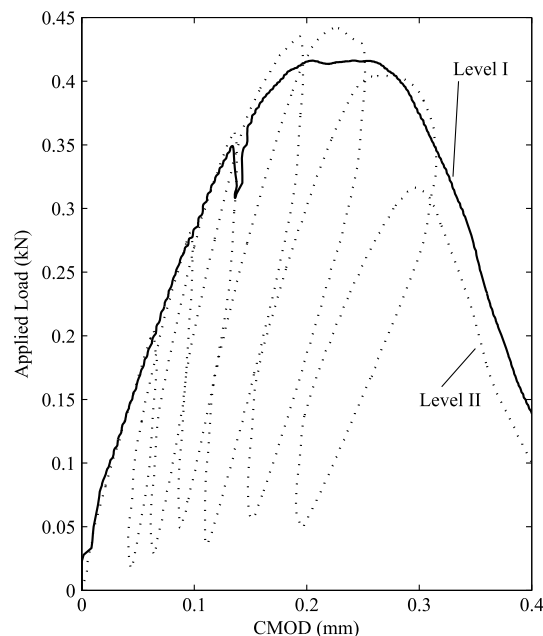


**Figure 7.** Example Level I (solid) and Level II (dotted) records from samples of Clashach sandstone. During the Level I experiment, only the peak load is required. During the Level II experiments, the hysteresis during cyclic loading is used to calculate a ductility correction,  $m$ . The reloading cycles become progressively less steep, representing inelastic deformation within the material. Here we assume equivalence in peak load between the two experiment types and find  $K_{Ic}$  from the peak load during a Level II experiment.

at the ligament tip and propagate along the ligament, increasing in width as it grows. Crack propagation is initially stable because although the stress intensity factor increases with the increasing crack length, the energy required to propagate the fracture initially increases faster due to the increasing width of the fracture [Ouchterlony, 1989; Rist et al., 2002; Cui et al., 2010]. At a known crack length [see ISRM, 1988] the increase in stress intensity factor becomes dominant over the increase in required energy, and the propagation then becomes unstable (dynamic). The peak load occurs at the instability point, and the fracture toughness,  $K_{Ic}$ , is calculated from this peak value and the specimen dimensions according to

$$K_{Ic} = \frac{A_{min} F_{max}}{D^{1.5}} \quad (2)$$

where  $A_{min}$  is a dimensionless constant calculated from the critical crack length. ISRM [1988] and Ouchterlony [1989] find  $A_{min}$  to be equal to 24.0.

Measurement of the fracture toughness in this way is known as Level I testing and inherently assumes a linear elastic fracture mechanics (LEFM) approach and that the samples are ideally brittle. However, it is well established that most rocks do not behave in an ideally linear elastic manner and exhibit some ductility (see compilation in Meredith [1989]). Under these circumstances, the LEFM assumption becomes invalid. However, the extent of the nonlinearity (ductility) can be determined by Level II testing, which makes use of the extended period of stable crack growth noted above. Here the sample is cyclically loaded and unloaded a number of times, inducing sequential increments of crack extension. The crack mouth opening displacement (CMOD) is measured with linear variable differential transducers (LVDTs) and the crack tip position inferred from the specimen compliance.

Examples of both a Level I test and a Level II test with six unloading cycles on short-rod samples of Clashach sandstone are shown in Figure 7.

Level II testing requires continuous monitoring of the load and displacement throughout the test and allows a correction to be made for inelastic deformation around the crack tip. Fracture toughness values incorporating this correction are referred to as  $K_{Ic}^c$ . Cui et al. [2010] note that substantially less scatter is observed in  $K_{Ic}^c$  than in  $K_{Ic}$ .

The sample is cyclically loaded under LVDT displacement control of the jaw movement. An example load-displacement curve for Clashach sandstone is plotted in Figure 7. A constant displacement rate of  $0.002 \text{ mm s}^{-1}$  was used for both the loading and unloading of the samples, and samples were not fully unloaded to avoid potential movement within the loading grips and the potential for backlash in the loading system producing additional hysteresis. Experiments were conducted on Darley Dale and Clashach sandstones to confirm that the measured fracture toughness was not dependent on the displacement rate. For this study, the Level I fracture toughness was determined from the peak load during a Level II cyclically loaded experiment. Tests were conducted on Darley Dale and Clashach sandstones in order to verify that the peak load is equivalent between Level I and Level II experiments. While the location of a progressing crack tip is well defined, nonbrittle processes around the tip lead to a residual displacement after the material is unloaded. As a result, the unloading/reloading cycle does not lie exactly parallel to the initial loading curve [Ouchterlony, 1989]. Barker [1979] defines a degree of nonlinearity,  $p$ , which can be calculated from the gradients of sequential loading cycles according to the method described by ISRM [1988]. Each loading cycle is linearized and extrapolated to the peak load, and the zero load line,  $p$ , is then equal to the ratio of the CMOD change between cycles at peak load and the CMOD change at zero load,  $p = \delta_{\text{CMOD,peak}} / \delta_{\text{CMOD,zero}}$ . The factor  $m = \sqrt{(1+p)/(1-p)}$  then relates the Level II fracture toughness,  $K_{\text{Ic}}^{\text{c}}$  to the Level I value  $K_{\text{Ic}}^{\text{c}}$  by  $K_{\text{Ic}}^{\text{c}} = mK_{\text{Ic}}^{\text{c}}$  and is hereon referred to as a ductility correction factor [Meredith, 1989]. For a purely linear elastic material,  $m = 1$ , and a larger value of  $m$  implies that the material behavior is farther from linear elasticity. The maximum value listed by ISRM [1988] is  $m = 1.88$ , reported by Schmidt and Huddle [1977a] on Anvil Points oil shale.

ISRM [1988] lists additional quantities that can be determined from a loading curve if the absolute displacement is known. The Young's modulus in bending,  $E$  (in GPa), can be determined according to

$$E = C_E \frac{84.5s_{\text{init}}}{D} \quad (3)$$

where  $s_{\text{init}}$  is the initial gradient of the curve in kN/mm and  $D$  is the sample diameter in mm.  $C_E$  is a correction factor given by

$$C_E = 1 + \frac{2.9\Delta a_0}{D} + 2.5 \left( \frac{t}{D} - 0.012 \right) \quad (4)$$

where  $t$  is the notch width and  $\Delta a_0$  is the uncertainty in  $a_0$  (each in millimeters). Assuming  $\Delta a_0 \simeq 1 \text{ mm}$ ,  $C_E$  is equal to 1.1. The critical energy release rate can then be calculated from

$$G_{\text{SR}}^{\text{c}} = \frac{(1 - \nu^2)(K_{\text{Ic}}^{\text{c}})^2}{E} \quad (5)$$

where  $\nu$  is Poisson's ratio. Here we assumed that  $\nu \simeq 0.25$ .

Following ISRM [1988], Hanson and Ingraffea [1997], and Bartsch et al. [2004], the specific work of fracture,  $\bar{R}_{\text{SR}}$  (joule  $\text{m}^{-2}$ ), can be determined by dividing the integral over the loading curve by the fracture area:

$$\bar{R}_{\text{SR}} = \frac{\int_0^{\text{CMOD}_{\text{peak}}} Pd(\text{CMOD})}{A_c} \quad (6)$$

where  $\text{CMOD}_{\text{peak}}$  is the CMOD value at which the peak load occurs,  $P$  is the load applied during the experiment, and  $A_c$  is the cracked area of the ligament at peak load. The specific work of fracture is expected to correlate closely with the critical energy release rate [Hanson and Ingraffea, 1997]. We cannot directly determine the cracked area during the experiment, so we assume that the crack front is straight and that the peak load occurs at  $a = a_c$ . From Figure 8, we see that for a fracture of length  $a_c$ , the fracture area is given by

$$A_c = (\alpha_c - \alpha_0)^2 D^2 \tan \theta \quad (7)$$

For samples with  $D = 60 \text{ mm}$  and  $\alpha_0 = 0.45D$  and  $\alpha_c = 0.91D$ ,  $A_c$  is found to be  $3.43 \times 10^{-4} \text{ m}^2$ . The loading curves plotted throughout this project have units of kilonewton and millimeter, so an integral in these units is equivalent to Newton Metres (N.m.) or Joule (J.) The integral,  $\int_0^{\text{CMOD}_{\text{peak}}} Fd\text{CMOD}$  is approximated numerically

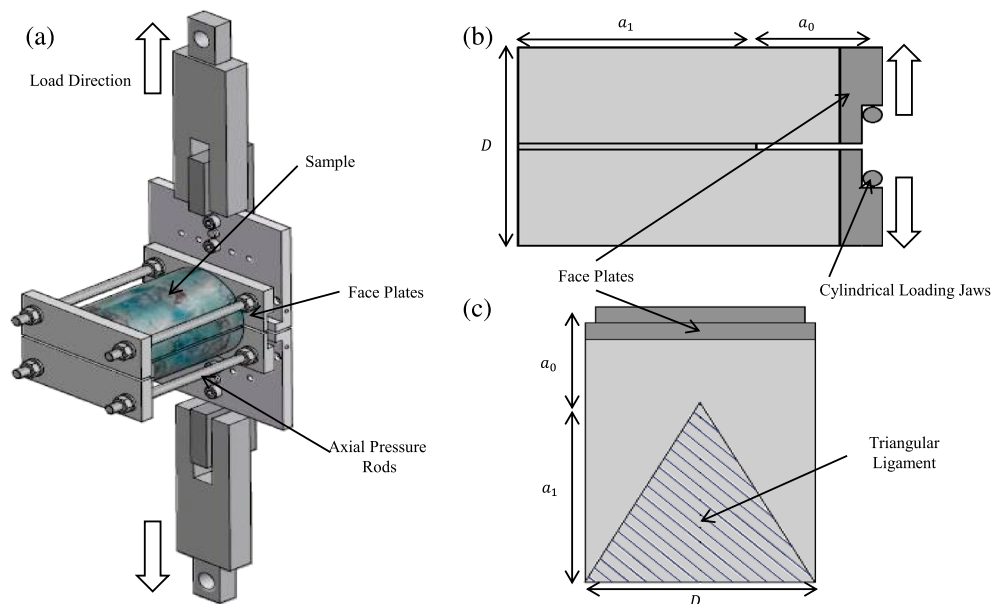


**Figure 8.** The experimental setup used for short-rod experiments on the Mancos shale. The bottom jaw is fixed in place, and the upper jaw is raised. Displacement transducers mounted on the rear of the jaws shown in Figure 8a are used to monitor the crack mouth opening displacement and are used to control the displacement rate. The face plates are seen on the front of the sample, abutting the jaws. The axial pressure modification is seen in the studding connecting the face plates and rear plates. The nuts on the rear plates are tightened with a torque wrench, so that a known axial pressure is applied. Note that the front and rear plates cover the entirety of each side of the notch, so that the axial pressure is applied over the entire region up to the notch. Image and design by N. Hughes.

from the loading curve by removing the loading cycles before using the trapezium rule on the cycle-less loading curve. The specific work of fracture,  $\bar{R}_{SR}$ , is then found from equation (6).

The standard short-rod methodology as laid out by *ISRM* [1988] and described above was used for experiments on all test materials other than Mancos shale. A number of modifications to the methodology were required in order to perform successful experiments on the shale.

Figure 8 shows the specimen geometry used for all of the measurements on Mancos shale described in this study. This setup has the same geometry as is recommended by *ISRM* [1988], but there are some differences in terms of arrangement. The standard methodology of loading against the rock material at the corners of the loading groove is not suitable for Mancos shale because fractures were found to develop from the loading points. We therefore load against metal jaws while ensuring that all dimensions remain the same. The load is transmitted via cylindrical loading bars to ensure a perfect line contact.

In the Arrestor orientation we commonly observe premature transverse tensile failure of our short-rod samples. Such failure occurs during loading when the propagating crack deviates from the ligament plane, normal to bedding, and into the bedding plane. This occurs due to a combination of tensile bending stresses within the short-rod arms and the anisotropy of the fracture toughness. The bedding layers provide planes of weakness, causing the sample to fail transversely at a shorter crack length than is required to evaluate the fracture toughness,  $a_{max}$  [Ingraffea et al., 1984]. Figure 9 shows an Arrestor-orientation sample of the Mancos shale where this deflection has occurred. Ingraffea et al. [1984] observed the same phenomenon in Indiana limestone and applied an axial pressure perpendicular to the sample axis, in order to prevent premature transverse tensile failure. The same method was used here, with loading plates attached to the steel loading jaws by lengths of studding (Figure 8). A torque wrench was used to apply a known axial pressure to the sample via the studding. An axial pressure of 1.6 MPa was found to be sufficient to prevent premature transverse tensile failure in the Arrestor orientation and is approximately 2% of the Mancos shale's compressive strength. Ingraffea et al. [1984] note that this axial pressure might be expected to affect the measured fracture toughness of the material. In order to investigate this possibility, short-rod experiments were conducted on Darley Dale and Crab Orchard sandstones, with a range of different axial pressures. The results of this investigation



**Figure 9.** An Arrestor-orientation short-rod sample which has succumbed to transverse tensile failure. The fracture has progressed along the chevron plane until it reaches a point where less energy is required to propagate the fracture perpendicular to the axis of the cylinder. This occurred commonly during Arrestor-orientation experiments. This is a manifestation of the same effect as is seen to divert the Arrestor orientation cracks during Brazilian Disk tests in Figure 6.

measurements on equivalent materials exist. Our  $K_{Ic}$  value for Carrara marble is higher than that reported by Meredith [1989] but agrees well with that of Migliazza *et al.* [2011] and ISRM [1988]. Our Indiana limestone value is substantially lower than those measured by Schmidt and Huddle [1977b] and Lim *et al.* [1994] but agrees closely with that reported by Abou-Sayed [1977]. Our  $K_{Ic}$  values for Crab Orchard (Tennessee) sandstone and Sölnhofen Limestone are significantly lower than the values reported by Meredith [1989]. For the materials listed in Table 5, our ductility correction factors,  $m$ , range between 1.13 for Indiana limestone and 1.67 for Crab Orchard sandstone.

are set out in Appendix A. The application of an axial pressure was found to have only a negligibly small effect on the measured value of  $K_{Ic}$  and to have no effect on  $K_{Ic}^C$ .

Loading of the sample was achieved using a 5 kN load cell within a uniaxial loading frame. The 60 mm diameter short-rod samples were manufactured in order to span multiple grain diameters, and so that the process zone size is small compared to the sample. All other proportions are as described by ISRM [1988]. Experiments were conducted on dry samples.

#### 4. Results: Fracture Toughness of the Mancos Shale and Comparison Materials

Fracture toughnesses for Mancos shale and the other comparator materials were measured using the methodologies described above. For Mancos shale, both  $K_{Ic}$  and  $K_{Ic}^C$  were determined in all three principal orientations. Table 5 lists the measured fracture toughness values, ductility correction factors, and the two energy estimates for all three orientations within Mancos shale and for the range of other sedimentary and carbonate comparator materials. Experiments were considered invalid if the crack deviates from the notch plane by more than 5 mm during an experiment; this is a slightly less stringent criterion than that suggested by ISRM [1988].

The fracture toughness values in Table 5 are generally seen to be similar in range to those reported by other authors, where

**Table 5.** Mean Fracture Toughness, Ductility Correction, and CMOD<sub>peak</sub> Values for a Variety of Rock Materials Including the Mancos Shale<sup>a</sup>

Material	$K_{Ic}$ (MPa m <sup>1/2</sup> )	$K_{Ic}^C$ (MPa m <sup>1/2</sup> )	$m$	$E$ (GPa)	$G_c$ (joule m <sup>-2</sup> )	$\bar{R}_{SR}$ (joule m <sup>-2</sup> )	$n_{repeats}$
Mancos shale (Divider)	0.44 ± 0.05	0.72 ± 0.17	1.62 ± 0.15	21 ± 3	27 ± 3	168 ± 54	3
Mancos shale (Short Transverse <sub>low</sub> )	0.12 ± 0.02	0.21 ± 0.02	1.83 ± 0.22	8 ± 1	6 ± 3	26 ± 7	5
Mancos shale (Short Transverse <sub>high</sub> )	0.31 ± 0.01	0.52 ± 0.04	1.69 ± 0.15	12 ± 1	19 ± 5	103 ± 8	2
Mancos shale (Arrestor)	0.44 ± 0.07	0.65 ± 0.16	1.49 ± 0.37	11 ± 3	38 ± 29	234 ± 140	3
Carrara marble	1.12 ± 0.06	1.39 ± 0.01	1.24 ± 0.07	36 ± 4	47 ± 5	204 ± 7	3
Darley Dale sandstone	0.56 ± 0.06	0.80 ± 0.023	1.44 ± 0.137	22 ± 5	33 ± 19	205 ± 51	5
Clashach sandstone	0.73 ± 0.18	1.04 ± 0.18	1.42 ± 0.141	15 ± 4	75 ± 41	293 ± 28	7
Crab Orchard sandstone	0.53 ± 0.00	0.88 ± 0.00	1.67 ± 0.00	30 ± 3	23 ± 2	422 ± 24	3
Portland limestone	0.56 ± 0.06	0.71 ± 0.07	1.27 ± 0.08	15 ± 6	32 ± 5	97 ± 8	3
Sölnhofen limestone	0.92 ± 0.04	1.27 ± 0.07	1.39 ± 0.131	33 ± 16	55 ± 37	129 ± 19	3
Indiana limestone	0.48 ± 0.05	0.54 ± 0.010	1.13 ± 0.09	28 ± 5	10 ± 2	51 ± 7	3

<sup>a</sup>Additionally, the Young's modulus in bending and both fracture energy estimates are listed.

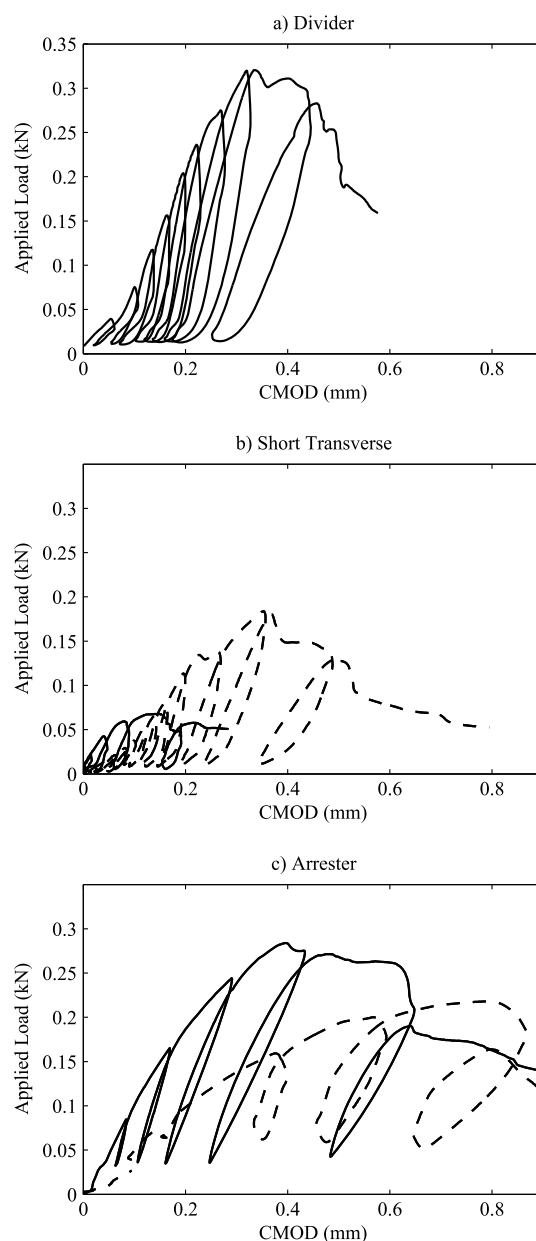


**Figure 10.** Example load-CMOD curves from Level II short-rod experiments conducted on Mancos shale in the Divider, Short Transverse, and Arrester orientations (Figures 10a–10c, respectively). Two distinct forms were repeatedly recorded in the Short Transverse orientation. In the Arrester orientation the peak load was consistent, but the loading curves demonstrated a wide variety of forms. Two examples are shown here.

An example Divider orientation load-CMOD curve for Mancos shale is plotted in Figure 10a. Eight loading/unloading cycles were completed during this experiment. A decreasing gradient and significant hysteresis can be observed for each successive cycle. In this experiment, peak load and  $\text{CMOD}_{\text{peak}}$  were measured as 0.33 kN and 0.32 mm, respectively. Over the three repeat experiments, the mean  $K_{\text{IC}}^{\text{c}}$  was calculated as  $0.44 \pm 0.08 \text{ MPa m}^{1/2}$ . Mean  $K_{\text{IC}}^{\text{c}}$  was calculated as  $0.72 \pm 0.17 \text{ MPa m}^{1/2}$ . Mean  $G_{\text{c}}$  was calculated to be  $27 \pm 3 \text{ joule m}^{-2}$  and mean  $R_{\text{SR}}$  was calculated to be around six times larger, at  $168 \pm 5 \text{ joules m}^{-2}$ .

As with the tensile strength, two distinct clusters of data are observed in the Short Transverse orientation, and an example load-CMOD curve from each data cluster is plotted in Figure 10b. For the lower curve, three loading cycles were completed, and peak load and  $\text{CMOD}_{\text{peak}}$  were measured as 0.07 kN and 0.14 mm, respectively. For the higher curve, it was possible to complete 11 loading cycles, and peak load and  $\text{CMOD}_{\text{peak}}$

were measured as 0.18 kN and 0.35 mm, respectively. Mean  $K_{Ic}$  values for each cluster were measured as  $0.12 \pm 0.02$  MPa m<sup>1/2</sup> and  $0.31 \pm 0.01$  MPa m<sup>1/2</sup>, respectively. The corresponding mean  $K_{Ic}^c$  values were calculated as  $0.21 \pm 0.02$  MPa m<sup>1/2</sup> and  $0.52 \pm 0.04$  MPa m<sup>1/2</sup>. Additionally, each cluster also corresponds to a different value of  $m$ , with the lower  $K_{Ic}$  corresponding to a higher value of  $m$ . In these experiments, values in the lower  $K_{Ic}^c$  cluster were recorded 5 times, and values in the higher  $K_{Ic}^c$  cluster only twice. Mean  $G_{c(\text{low})}$  was calculated to be  $6 \pm 3$  joule m<sup>-2</sup>, and mean  $\bar{R}_{SR(\text{low})}$  was measured as  $26 \pm 7$  joule m<sup>-2</sup>. Mean  $G_{c(\text{high})}$  was calculated to be  $19 \pm 5$  joule m<sup>-2</sup>, and mean  $\bar{R}_{SR(\text{high})}$  was calculated as  $103 \pm 8$  joule m<sup>-2</sup>.

An example Arrester orientation load-CMOD curve is plotted in Figure 10c. In this experiment the axial pressure modification described in section 3 was used to enable the fracture to propagate successfully across the sample. The modification resulted in successful fracture propagation in three out of four experiments conducted in this orientation. In this experiment, peak load and CMOD<sub>peak</sub> were measured as 0.28 kN and 0.39 mm, respectively. Mean  $K_{Ic}$  was measured as  $0.44 \pm 0.07$  MPa m<sup>1/2</sup>. Mean  $K_{Ic}^c$  was measured as  $0.65 \pm 0.16$  MPa m<sup>1/2</sup>. Mean  $G_c$  was calculated to be  $38 \pm 29$  joule m<sup>-2</sup>, and mean  $\bar{R}_{SR}$  was measured as  $234 \pm 140$  joule m<sup>-2</sup>.

## 5. Discussion

### 5.1. Mechanical Anisotropy

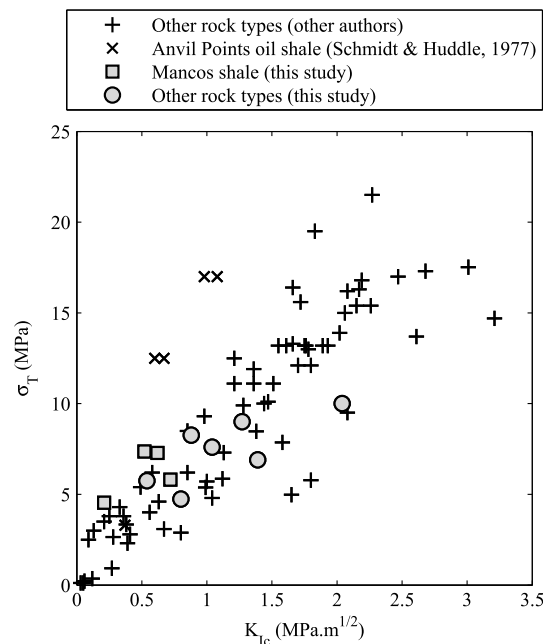
Mechanical anisotropy within shale material is expected to be caused by a combination of aligned clay material and organic materials, lamination (textural anisotropy), and microcracks oriented preferentially parallel to the layering of the material [Nadeau and Reynolds, 1981]. The substantial decrease in  $\epsilon$  with fluid saturation suggests that at least some of the observed anisotropy is caused by bedding-parallel microcracks, as saturation causes a much larger increase in  $v_p$  normal to the bedding than parallel [Pyrak-Nolte et al., 1990].

Table 5 lists the mean fracture toughness values in each of the three principal crack orientations described in section 2.4, as well as a range of other materials for comparison.  $K_{Ic}^c$  for the Mancos shale is seen to vary between 0.21 and 0.72 MPa m<sup>1/2</sup>, making it comparable to some of the weaker shales discussed by Chong et al. [1987] and to the Marcellus shale values reported by Lee et al. [2015]. Schmidt and Huddle [1977a] report slightly higher  $K_{Ic}$  values for the Anvil Points oil shale, and our values are also substantially lower than that reported for Mancos shale by Warpinski and Smith [1990].

The same general anisotropy is observed as in the Anvil Points oil shale by Schmidt and Huddle [1977a], with  $K_{Ic}^c$  slightly higher in the Divider orientation than the Arrester orientation and both being significantly higher than the Short Transverse orientation. It is only the lower of the two Short Transverse orientation measurements that falls significantly outside of the range observed for other materials. The  $m$  values are among the highest ductility corrections measured (by comparison with the other materials listed in Table 5) suggesting that the shale material behaves very inelastically.

As the crack progresses in the Divider orientation, it is simultaneously sampling multiple layers within the material. This can be thought of as a form of averaging, and as a result this orientation is the most commonly quoted in published literature for comparison between materials [Chong et al., 1987; Krishnan et al., 1998]. Some scatter in the recorded fracture toughness and tensile strength is expected because the thickness and distribution of specific layers varies substantially between samples. Therefore, a sample featuring proportionally more of the weaker material should be expected to have a lower fracture toughness and vice versa. This is illustrated by the largest standard deviation on our mean shale  $K_{Ic}^c$  measurements being recorded in this orientation.

In the Short Transverse orientation, both the propagation direction and crack plane are parallel to the bedding plane. In the case of horizontal bedding, this orientation models a crack propagating horizontally along a bedding plane. Because the crack propagation direction and crack plane are both parallel to the bedding layers, the crack could only ever sample one bedding plane for an ideal material. A bimodal distribution is observed in all of  $\sigma_T$ ,  $K_{Ic}$  and  $m$  (and consequently,  $K_{Ic}^c$ ). For both  $K_{Ic}^c$  and  $\sigma_T$ , the standard deviation on each cluster of values is very low which leads to the interpretation as a bimodal distribution and supports the idea that Divider and Arrester measurements sample a mixed material, but the Short Transverse measurements do not. Out of seven Short Transverse measurements, five samples were in the lower value cluster, and two were in the higher values cluster. The lower  $K_{Ic}$  mode is associated with a larger value of  $m$ , indicating that during the weaker mode the material behaves more inelastically. One possible interpretation of this bimodality of



**Figure 11.** Tensile strength as a function of fracture toughness for a wide variety of rocks. Data points are from Zhang [2002], with the exception of the additional points from this study. Where  $\sigma_T$  was not measured here, the values used are listed in Table 6. A linear regression finds  $\sigma_T = 6.76 K_{Ic}$ .

$\sigma_T$ ,  $K_{Ic}$ , and  $m$  relates to the fracture propagating through either of the two different types of layer within the shale. The weaker layers correspond to a higher value of  $m$ , because they are made up of weak, ductile clay. Visual inspection of fractured samples did not allow us to confirm this, because in most instances, the fracture propagated along or very close to layer interfaces.

In the Arrestor orientation, the crack propagates in a direction perpendicular to the bedding planes. In the case of horizontal bedding, this orientation models a crack propagating vertically. As the crack is propagating perpendicular to the layering, the crack tip is only sampling a single layer at any given time, so that while it samples each layer in the material, it does this sequentially. The variation in the loading curve was expected because in this orientation the crack front will only be encountering one layer of bedding at a time, so the crack resistance will vary as a function of the crack length and will differ depending on the specific layers in each sample.

The large scatter on the measured value of  $m$  may also be explained by the sequential sampling of the layers within the material. As the sample is unloaded, the effective crack tip passes through different layers. Therefore, the form of the unloading/reloading cycles should vary between samples, depending on what specific combination of layers is present.

### 5.2. Relationship Between Fracture Toughness and Tensile Strength

Zhang [2002] suggest that mode I fracture toughness and tensile strength should be related under quasi-static loading because in each case the tensile fracture occurs due to the extension of a single crack, and the fracture surfaces are often similar. Figure 11 shows the data compiled by Zhang [2002] along with the  $K_{Ic}^c$  values from this study and associated  $\sigma_T$  values listed in Table 6.

From the Griffith criterion [Paterson and Wong, 2005]

$$\sigma_T = C \frac{K_{Ic}}{\sqrt{a}} \tag{8}$$

where  $C$  is a dimensionless geometric factor and  $a$  is a characteristic flaw size. The dependence of  $\sigma_T/K_{Ic}$  on  $a$  is through an inverse square root so is expected to be quite small, but even so, the consistent slope in Figure 11 suggests that this characteristic flaw size is reasonably consistent between different rock types. The data for all three orientations in the Mancos shale sit on the main trend, but the Anvil Points oil shale results of

**Table 6.** Fracture Toughness and Tensile Strength Values for the Rock Materials Used in This Study<sup>a</sup>

Material	$K_{Ic}^c$ (MPa m <sup>1/2</sup> )	$\sigma_T$ (MPa)	$\sigma_T$ Reference
Mancos shale (Divider)	0.72	5.81	This Study
Mancos shale (Arrester)	0.62	7.28	This Study
Mancos shale (Short Transverse <sub>low</sub> )	0.21	4.54	This Study
Mancos shale (Short Transverse <sub>high</sub> )	0.52	7.36	This Study
Lanhelin granite	2.04	10.00	Homand et al. [2001]
Carrara marble	1.39	6.90	Wong et al. [2014]
Darley Dale sandstone	0.80	4.74	Vanichkobchinda et al. [2007]
Clashach sandstone	1.04	7.60	Crawford et al. [1995]
Crab Orchard sandstone	0.88	8.27	Weinberger et al. [1994]
Sölnhofen limestone	1.27	9.00	Migliazza et al. [2011]
Indiana Limestone	0.54	5.75	Weinberger et al. [1994]

<sup>a</sup>Where tensile strength was not measured as part of this study, a value from existing literature has been used.

Schmidt and Huddle [1977a] are characterized by a significantly higher  $\sigma_T/K_{Ic}$  ratio, potentially corresponding to a lower characteristic flaw size.

### 5.3. Inelasticity During Fracture Toughness Experiments

The Mancos shale  $K_{Ic}^c$  values reported in section 4 are not significantly lower than those found in other sedimentary materials but are strongly anisotropic, with  $K_{Ic,D}^c/K_{Ic,ST(low)}^c = 3.43$ . The ductility correction,  $m$ , is seen to vary between 1.49 and 1.83 for the Mancos shale, with the highest value corresponding to the low  $K_{Ic}$  value in the Short Transverse orientation. These values bracket the value of  $m = 1.73$  suggested by Barker and Guest [1978] and Costin [1981] as a maximum for validity of the method. Similar to the data of Costin [1981] for Anvil Points oil shale, we also note that the highest  $m$  value for Mancos shale is above the limit and occurs in the Short Transverse orientation. However, we also note that the values are not significantly higher than those recorded for other sedimentary rocks. For example, the  $m$  value for Crab Orchard sandstone is 1.67.

These high  $m$  values suggest significant inelasticity, and we might therefore expect the results to exhibit some scale dependence. Grant et al. [2000] demonstrated for the short-rod specimen geometry that  $m$  values decreased with increasing specimen size up to some critical diameter. If the size of the inelastic process zone is not negligible relative to the sample size, then yielding at the crack tip is not completely suppressed as would be the case in true plane strain conditions. If this is the case for our samples, in spite of their relatively large 60 mm diameter, then our calculated  $K_{Ic}^c$  values will be overestimated [Wang and Pilliar, 1989].

These factors suggest that the values of both  $K_{Ic}$  and the ductility factor  $m$  presented here should be thought of as maximum bounds for the true values. Significantly, the  $m$  value corresponding to the low Short Transverse orientation  $K_{Ic}$  is the highest value recorded here ( $m_{ST(low)} = 1.83$ ) and is significantly higher than that recorded in either the Divider or Arrester orientation (1.62 and 1.49, respectively). Increasing  $m$  values are expected to lead to increasing process zone sizes [Grant et al., 2000], and therefore, we might assume that the  $K_{Ic}$  values corresponding to higher  $m$  values are likely overestimated by more than those associated with lower  $m$  values. If this is the case, then the lowest  $K_{Ic}^c$  value;  $K_{Ic,ST(low)}^c (=0.21 \text{ MPa m}^{1/2})$  is likely more of an overestimate than the highest value;  $K_{Ic,D}^c (=0.72 \text{ MPa m}^{1/2})$ . Therefore, while the  $K_{Ic}^c$  values presented here ought to be regarded as maximum bounds, the  $K_{Ic}^c$  anisotropy should potentially be regarded as a minimum.

### 5.4. Implications for Crack Propagation Under Mixed-Mode Loading

During both the tensile strength and fracture toughness experiments discussed here, we observe a tendency for fractures propagating in the Arrester orientation to become deflected into the Short Transverse orientation and become trapped there. Furthermore, we observe a general tendency of the fractures to be tortuous and kinked (although no attempt was made to quantify fracture roughness systematically). If this behavior is replicated in nature, then fractures initiated perpendicular to the bedding might be expected to deflect along the bedding planes and remain in this propagation direction for some distance. While there are three classical criteria for analyzing deflection of the crack path, namely, the maximum energy release rate, the maximum hoop stress, and the zero mode II stress intensity factor criteria, it is impossible to choose between the three

based on our experimental data alone. We therefore follow *Lawn* [1993] and choose the maximum energy release rate criterion of *Nuismer* [1975]. This is also consistent with the work of *Lee et al.* [2015] on fracture-vein interaction in shale. As an investigation into the conditions under which this deflection may occur, here we use our anisotropic fracture toughness data for Mancos shale to make predictions of crack deflection based on the maximum energy release rate criterion of *Nuismer* [1975].

#### 5.4.1. Crack Kinking Analysis Accounting for Elastic Anisotropy

*Hutchinson and Suo* [1992] present a crack kinking analysis for elastically orthotropic materials. This methodology is only able to investigate cracks kinking through exactly  $90^\circ$ , so here we consider cracks initially propagating in the Arrester orientation and potentially deflecting into the Short Transverse orientation.

$G_c$  is calculated as  $G_c = (1 - \nu^2)K_{Ic}^2/E$ , and the stiffness matrix,  $c$ , is constructed from the values in Table 3. The compliance matrix,  $s$ , is then found by  $c^{-1}$ .

Following *Hutchinson and Suo* [1992], crack deformation in the (1, 2) plane (with the one direction bedding perpendicular) satisfies

$$\epsilon_i = \sum_{j=1,2,6} b_{ij}\sigma_j, \quad i = 1, 2, 6 \quad (9)$$

for  $i, j = 1, 2, 6$ , where

$$b_{ij} = \begin{cases} s_{ij}, & \text{(plane stress)} \\ s_{ij} - \frac{s_{i3}s_{j3}}{s_{33}}, & \text{(plane strain)} \end{cases} \quad (10)$$

so that there are only four independent elastic constants:  $b_{11}$ ,  $b_{12} = b_{21}$ ,  $b_{22}$ , and  $b_{66}$  as  $b_{16} = b_{26} = 0$ . *Suo et al.* [1991] show that the stresses then depend on only two elastic parameters:

$$\lambda = \frac{b_{11}}{b_{22}} \quad (11)$$

and

$$\rho = \frac{b_{12} + \frac{b_{66}}{2}}{\sqrt{b_{11}b_{22}}} \quad (12)$$

The energy release rate for the crack to continue straight ahead is then given by

$$G = b_{11}n (\lambda^{-3/4}K_I^2 + \lambda^{-1/4}K_{II}^2) \quad (13)$$

where  $n = [(1 + \delta)/2]^{1/2}$ . *Suo et al.* [1991] show that for a crack kinking through  $90^\circ$ , the crack tip stress intensities are given by

$$K_I^t = p_{11}\lambda^{-3/8}K_I + p_{12}\lambda^{-1/8}K_{II} \quad (14)$$

$$K_{II}^t = p_{21}\lambda^{-1/8}K_I + p_{22}\lambda^{1/8}K_{II} \quad (15)$$

where the  $p_{ij}$ s are interpolated from a table listed in *Suo et al.* [1991] (who use  $c$ . Here we use  $p$  to avoid confusion with the stiffnesses). The energy release rate at the kinked crack tip is given by

$$G^t = b_{22}n (\lambda^{3/4}K_I^{t2} + \lambda^{1/4}K_{II}^{t2}) \quad (16)$$

and therefore,

$$\frac{G}{G^t} = \lambda^{1/4} \left[ \frac{1 + \zeta^2}{(p_{11}^2 + p_{21}^2) + 2\zeta(p_{11}p_{12} + p_{21}p_{22}) + \zeta^2(p_{12}^2 + p_{22}^2)} \right] \quad (17)$$

where  $\zeta = (\lambda^{1/4}K_{II})/K_I$ . The crack will then kink at  $90^\circ$  if

$$\frac{G}{G^t} \leq \frac{G_{c,A}}{G_{c,ST}} \quad (18)$$

Therefore, the kinking is dependent only on  $E$ ,  $\nu$ , the stiffness matrix, the ratio  $K_{Ic,A}/K_{Ic,ST}$ , and the loading conditions at the tip of the main crack,  $K_I, K_{II}$ . The values used here were  $E = 35.65$  GPa,  $\nu = 0.2$ ,

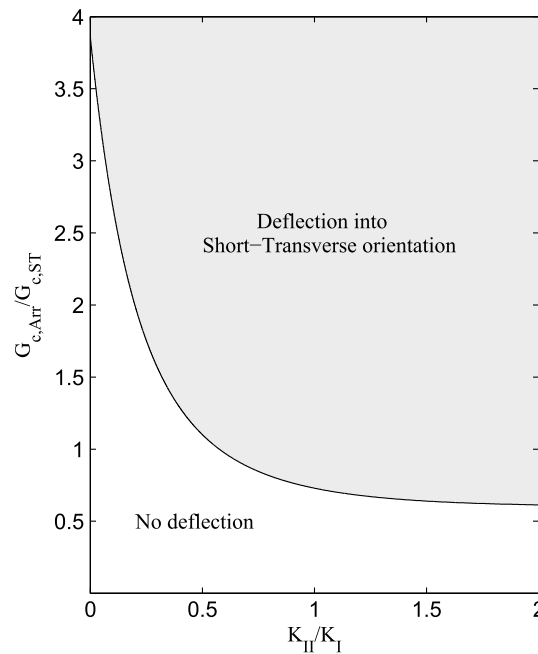


**Figure 12.** Parameter space in terms of  $K_{II}/K_I$  ratio and  $G_{c,A}/G_{c,ST}$  ratio, plotting whether or not a crack traveling in the Arrester orientation will deflect into the Short Transverse orientation. This particular figure was determined for dry material under plane strain, but the differences observed between dry and wet material, plane stress, and plane strain were negligible.

$K_{Ic,A} = 0.65 \text{ MPa m}^{1/2}$ ,  $K_{Ic,ST,low} = 0.21 \text{ MPa m}^{1/2}$ ,  $K_{Ic,ST,high} = 0.52 \text{ MPa m}^{1/2}$  as found for Mancos shale and listed in Tables 1 and 6.

The difference between plane stress and plane strain (through equation (10)) is seen to be negligible here. The difference between the result using the dry or saturated elastic constants from Table 3 is also seen to be negligible. Figure 12 shows the parameter space in terms of  $K_{II}/K_I$  ratio and  $G_{c,A}/G_{c,ST}$  ratio, plotting whether or not a crack traveling in the Arrester orientation will deflect into the Short Transverse orientation. Above a certain critical  $G_{c,A}/G_{c,ST}$  ratio (around 3.8), it is seen that the crack should always deflect into the Short Transverse orientation regardless of the loading conditions. For our results,  $G_{c,A}/G_{c,ST,high} = 1.56$  and  $G_{c,A}/G_{c,ST,low} = 9.58$ . Therefore, it should be expected that the crack will only deflect within the stronger beds when  $K_{II} > 0.3 K_I$ . Within the weaker beds, the crack should always deflect into the Short Transverse orientation regardless of the loading conditions.

**5.4.2. Crack Kinking Analysis With More General Incidence Angle and Loading Conditions**

The analysis above is useful for studying cracks kinking through exactly 90°, but notably, beds within shale formations are not completely planar and do not lie perfectly parallel to one another, so fractures propagating normal to the bedding at a large scale are not always propagating normal to the bedding at a local scale. Fractures are therefore expected to kink repeatedly, which is supported by visual inspection of our Arrester orientation samples that displayed tortuous crack paths with many smaller kinks. These smaller kinks can introduce nonzero  $K_{II}$  terms, even when the applied loading is purely opening mode. Therefore, here we present a second analysis, which is capable of dealing with cracks kinking at a range of angles and under a range of loading conditions but assumes elastic isotropy in the material. In this analysis we assume that the anisotropy in  $G_c$  is dominant over the effect of the elastic anisotropy in the material.

A small kink is assumed to develop at the tip of a progressing fracture, so that it will continue to propagate in mixed mode with kink-tip stress intensity factors  $K_{I,kink}$  and  $K_{II,kink}$ . The energy release rate is then given by

$$G(\theta) = \frac{1 - \nu^2}{E} (K_{I,kink}^2 + K_{II,kink}^2) \tag{19}$$

where  $\nu$  is Poisson’s ratio and  $E$  is Young’s modulus. The crack will propagate in the direction  $\theta$  which corresponds to the maximum energy release rate and will propagate unstably if  $G \geq G_c$ , the critical fracture energy.

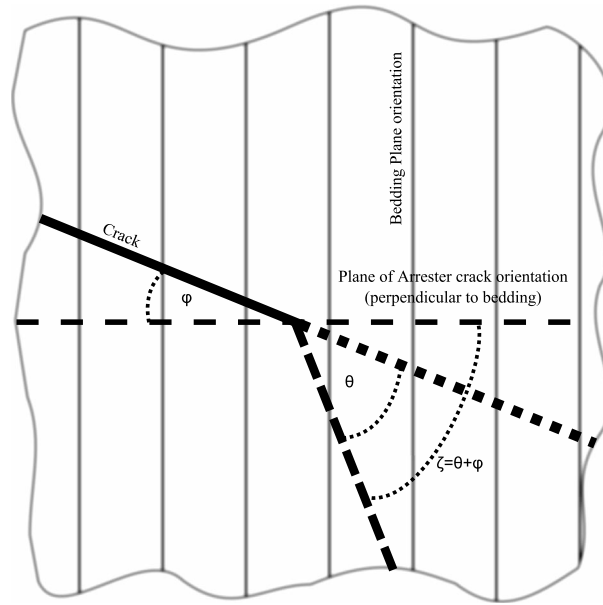


**Figure 13.** The notation used when describing crack tip deflection throughout this section.  $\phi$  is the angle between the incident fracture and the axis of symmetry (i.e., the Arrested orientation) in the material.  $\theta$  is the angle between the crack propagation direction and the direction of potential deflection.  $\zeta$  is the angle between potential deflection and the axis of symmetry (i.e.,  $\zeta = \phi + \theta$ ).

Here we calculate  $G_c$  according to

$$G_c = \frac{1 - \nu^2}{E} K_{Ic}^2 \tag{20}$$

using our anisotropic fracture toughness measurements for Mancos shale.  $G_c$  can therefore be calculated directly from the fracture toughness values found in section 4 and the bedding-parallel Poisson’s ratio and Young’s modulus values found in section 2.

No agreement exists in the literature about the variation of fracture toughness away from the principal crack orientations. Here we define  $\zeta$  as the angle from the Arrested orientation as shown in Figure 13, and we assume that  $G_c = G_{Ic,A}$  at all angles apart from  $\zeta = 90^\circ$ , where  $G_c = G_{Ic,ST}$ .  $G_c(\phi)$  is therefore a spike function as described in equation (21), with the required fracture energy equal in all orientations except directly along the bedding planes, where  $G_c(9^\circ)$  is significantly lower. This corresponds to a material with uniform fracture toughness except for a plane of weakness in the Short Transverse orientation.

$$G_c = \begin{cases} G_{Ic,A}, & \zeta \neq \pm 90^\circ \\ G_{Ic,ST}, & \zeta = \pm 90^\circ \end{cases} \tag{21}$$

This corresponds to the minimum possible effect of anisotropy so should serve as a suitable baseline with no further knowledge of the form of how  $K_{Ic}$  varies with  $\zeta$ .

*Cotterell and Rice* [1980] solve for the elastic stress-intensity factors,  $K_I$  and  $K_{II}$  at the tip of an infinitesimal kink in a two-dimensional crack from the stress intensities and surface tractions of the initiating kink. The kink stress intensity factors are given by

$$\begin{aligned} K_{I,kink} &= C_{11}K_I + C_{12}K_{II} \\ K_{II,kink} &= C_{21}K_I + C_{22}K_{II} \end{aligned} \tag{22}$$

where

$$\begin{aligned} C_{11} &= \frac{1}{4}(3 \cos(\theta/2) + \cos(3\theta/2)) \\ C_{12} &= -\frac{3}{4}(\sin(\theta/2) + \sin(3\theta/2)) \\ C_{21} &= \frac{1}{4}(\sin(\theta/2) + \sin(3\theta/2)) \\ C_{22} &= \frac{1}{4}(\cos(\theta/2) + 3 \cos(3\theta/2)) \end{aligned} \tag{23}$$

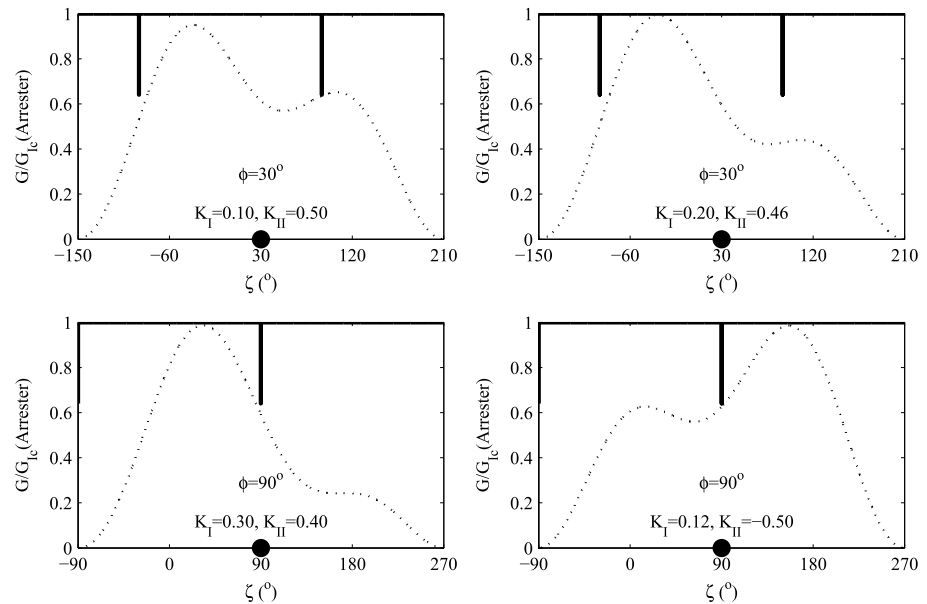


**Figure 14.** Example  $G$  and  $G_c$  curves around cracks oriented at different angles from bedding perpendicular ( $\phi$ ) and with different stress intensities,  $K_I$  and  $K_{II}$ . In each case, the dashed lines represent  $G(\zeta)$  around the crack tip, and the solid line plots the spike function fitted to  $G_c$  as described in equation (21). The higher of the two  $G_{Ic,ST}$  values is plotted here. The solid circle marks  $\phi$ , the angle from bedding perpendicular of the main crack as described in Figure 13. If the  $G(\zeta)$  curve reaches the spikes in  $G_c$  before the rest of the  $G_c$  function, the fracture might be expected to divert into the Short Transverse orientation.

and  $K_I, K_{II}$  are the stress-intensity factors of the main crack and  $\theta$  is the angle of the initiating kink from the main crack direction. Equations (22) and (23) are derived for an elastically isotropic material. *Cottrell and Rice* [1980] show that in the cases of mode I (i.e.  $K_{II} = 0$ ) and mode II loading of the main crack, these functions are accurate to within 5% and 10%, respectively, for angles up to  $\theta = 90^\circ$ .  $G_{kink}$  can then be calculated from equation (19) using  $K_{I,kink}$  and  $K_{II,kink}$ .

As stress intensity increases at a crack tip, the fracture will propagate in the direction where  $G$  first becomes equal to  $G_c$ . Figure 14 shows examples of  $G$  and  $G_c$  around a crack tip, as formulated from equations (19) and (21), respectively, with  $G_{Ic,ST} = G_{Ic,ST(low)}$ . With varying  $K_I, K_{II}, \phi, G_{Ic,A}$ , and  $G_{Ic,ST}$ , the first contact between the  $G$  and  $G_c$  curves occurs at different angles. *Lee et al.* [2015] use a similar type of analysis to investigate the kinking of shale fractures into cemented calcite veins. In their model, they assume that the bulk shale material is isotropic but contains a calcite vein that behaves similarly to the weak Short Transverse plane in our model, providing a spike function along the vein where  $G_c$  is lower than at other angles. The model presented here expands on that presented by *Lee et al.* [2015] by investigating the effect of nonzero  $K_{II}$  on crack deflection.

Figures 15 and 16 plot parameter spaces of the crack propagation criterion as a function of the main-crack stress intensity factors,  $K_I$  and  $K_{II}$  at varying angles of incidence to the Arrester orientation,  $\phi$ , using  $K_{Ic,ST} = K_{Ic,ST(low)}$  and  $K_{Ic,ST} = K_{Ic,ST(high)}$ , respectively. In Figures 15 and 16 the white regions represent  $K_I, K_{II}$  combinations for which failure will not occur, because  $G(\theta) < G_c(\zeta)$  for all  $\theta$ . The pale grey regions represent  $K_I, K_{II}$  combinations where  $G(\theta)$  reaches  $G_{Ic,ST}$  at  $\zeta = \pm 90^\circ$  before  $G(\theta)$  reaches  $G_c(\zeta)$  at any other angle, and the failure therefore occurs in the Short Transverse orientation. The dark grey regions represent  $K_I, K_{II}$  combinations where  $G(\theta)$  reaches  $G_{Ic,A}$  at some angle other than the Short Transverse orientation before  $G(\theta)$  reaches  $G_{Ic,ST}$  at  $\zeta = \pm 90^\circ$ , and the failure therefore occurs away from the Short Transverse orientation.

When  $K_{Ic,ST} = K_{Ic,ST(low)}$  (and therefore  $G_{Ic,ST} = G_{Ic,ST(low)}$ ), Figure 15 shows that this formulation predicts that the fracture can never propagate in any direction other than the Short Transverse orientation. When  $K_{Ic,ST} = K_{Ic,ST(high)}$ , (and therefore  $G_{Ic,ST} = G_{Ic,ST(high)}$ ), Figure 16 shows that the fracture may propagate either along or away from the Short Transverse orientation depending on the specific combination of  $K_I, K_{II}$ , and  $\phi$ . It should be noted that in reality the material will fail as soon as the combination of stress intensities reaches the boundary of the white region in Figures 15 and 16. Therefore, the grey shaded regions will never be reached

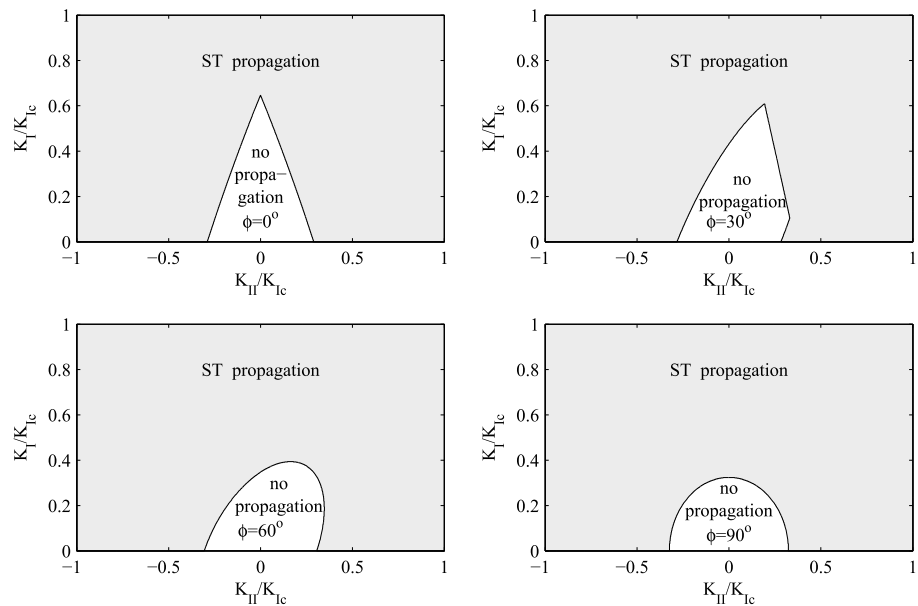


**Figure 15.** Propagation direction as a function of the main crack stress intensities,  $K_I$  and  $K_{II}$  for  $K_{Ic,ST} = K_{Ic,ST(low)}$ . The separate plots demark different angles of incidence,  $\phi$ , to the Arrestor orientation. At  $\phi = 0$ , the main fracture is propagating in the Arrestor orientation, and at  $\phi=90^\circ$ , the main fracture is propagating in the Short Transverse orientation. At all combinations where the stress intensities are high enough for the crack to propagate, propagation occurs in the Short Transverse orientation.

and should be thought of as simply demarking which regions of the boundary correspond to each crack propagation mode.

Figure 15 suggests that while using  $G_{c,ST(low)}$ , cracks should divert into the Short Transverse orientation and remain trapped there under all loading conditions. This agrees with the deflections into this orientation that were observed during experiments.

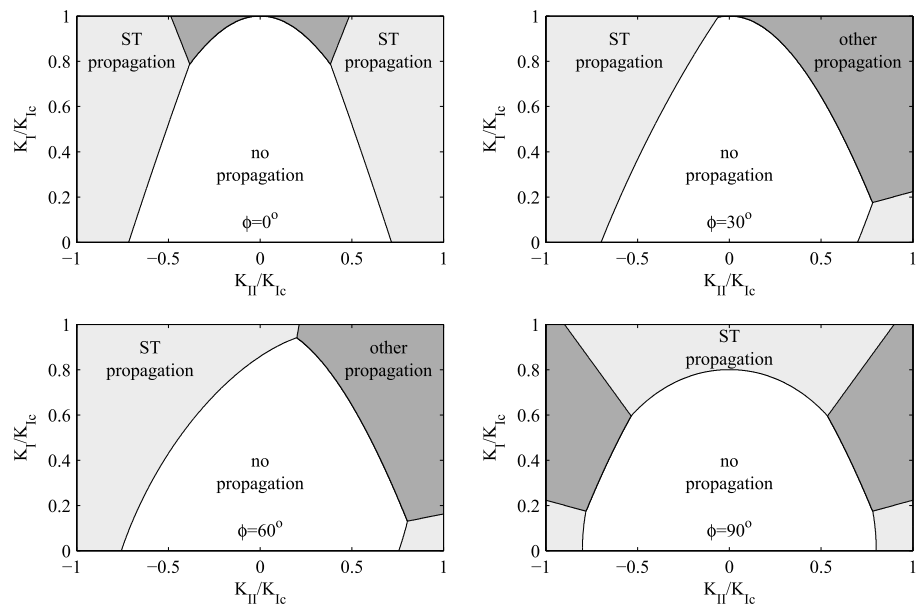


**Figure 16.** Propagation direction as a function of the main crack stress intensities,  $K_I$  and  $K_{II}$  for  $K_{Ic,ST} = K_{Ic,ST(high)}$ . The separate plots demark different angles of incidence,  $\phi$ , to the Arrestor orientation. At  $\phi = 0$ , the main fracture is propagating in the Arrestor orientation, and at  $\phi = 90^\circ$ , the main fracture is propagating in the Short Transverse orientation. The propagation mode varies as a function of  $\phi$ ,  $K_I$ , and  $K_{II}$ . A range of points from the boundaries are plotted in Figure 14.

With  $G_{c,ST} = G_{c,ST(\text{high})}$ , the toughness of the weak plane is closer to that in other orientations. While using  $G_{c,ST(\text{high})}$ , Figure 16 shows that the failure orientation varies as a function of the loading conditions. This implies that there is likely a threshold ratio of  $G_{c,ST}/G_{c,A}$  below which the Short Transverse orientation acts to strongly attract fractures.

In general, the results of this model suggest that fractures propagating within the shale are unlikely to be smooth. Fractures are able to kink at angles up to  $90^\circ$ , and the path is expected to be sensitive to both the loading conditions and the anisotropy in  $G_c$  (and therefore, fracture toughness). Therefore, in a heterogeneous material like shale, multiple kinks should be expected.

## 6. Conclusions

Fracture toughness has been determined under ambient conditions for the three principal crack orientations in Mancos shale. Two different clusters of  $K_{Ic}^c$  measurements are observed in the Short Transverse orientation. This behavior is also observed in tensile strength measurements recorded using the Brazilian disk methodology. There is significant anisotropy between the three orientations, with  $(K_{Ic}^c(D))/(K_{Ic}^c(ST_{\text{low}})) = 3.43$ . Nevertheless, the fracture toughness values are not unusually low, with only  $K_{Ic}^c(ST_{\text{low}})$  lying outside the range observed for other sedimentary materials.

The ductility correction factor,  $m$ , is seen to vary between 1.49 and 1.83 for the Mancos shale, with the highest value corresponding to the low  $K_{Ic}$  value in the Short Transverse orientation. These values bracket the value of  $m = 1.73$  suggested by *Barker and Guest* [1978] and *Costin* [1981] as a maximum for LEFM validity. Again though, these values are not significantly higher than those recorded in other sedimentary materials, with  $m(\text{Crab Orchard sandstone}) = 1.67$ . These high ductility values suggest that our fracture toughness values might be expected to exhibit some scale dependence. Therefore, they should be regarded as maximum bounds on the true  $K_{Ic}$  and  $m$  values but do provide the first accurate estimates for the order-of-magnitude of fracture toughness and mechanical anisotropy in a shale material of this type. In contrast, this same effect is believed to mean that the fracture toughness anisotropy is actually a minimum bound, as described in section 5.3. Therefore, this issue of inelasticity is something that should be addressed during further studies of fracture mechanics in sedimentary rocks.

A pair of simple models based on energy release rate have been used in combination with the anisotropic  $K_{Ic}^c$  measurements presented here to explain the deflection of fractures into the weaker Short Transverse orientation. They each demonstrate that fractures should always be expected to initially deflect into the weaker beds but will also deflect within the stronger beds under certain conditions. Because bedding in shale materials is unlikely to be perfectly parallel, fractures are expected to kink repeatedly and have a greater surface area than expected for a straight crack. This larger surface area could potentially correspond to more gas being accessed during hydraulic fracturing than the crack length alone would suggest. In the context of shale gas recovery by hydraulic fracturing, such a kink-enhanced increase in crack surface would be beneficial and potentially lead to increased gas recovery.

## Appendix A: Effects of the Axial-Pressure Modification on Measured Fracture Toughness

In section 3 we describe an axial pressure modification that was developed following [*Ingraffea et al.*, 1984]. *Ingraffea et al.* [1984] suggest that the application of an axial pressure is likely to affect the measured fracture toughness of the material due to the applied axial pressure being a significant proportion of the material's compressive strength. They observe a 5% decrease in the measured fracture toughness of Indiana limestone when applying an axial pressure of 8.35 MPa and a 1% decrease in Westerley granite. In order to use the axial-pressure methodology, it was therefore important to understand whether the axial pressure is affecting the measured fracture toughness. Due to the relative scarcity of the shale samples, it was decided to test this effect using Level-II experiments on Darley Dale and Clashach sandstones. Additionally, Level-II experiments were conducted on the anisotropic Crab Orchard sandstone in the Arrester orientation with the aim of characterizing whether the axial pressure affected an anisotropic material differently, as this modification would be used in the Arrester orientation on the Mancos shale.

In order to account for the effects of applying an axial pressure, axial pressures ranging between 0.6 and 2.5 MPa were applied to short-rod samples before measuring fracture toughness using the methodology

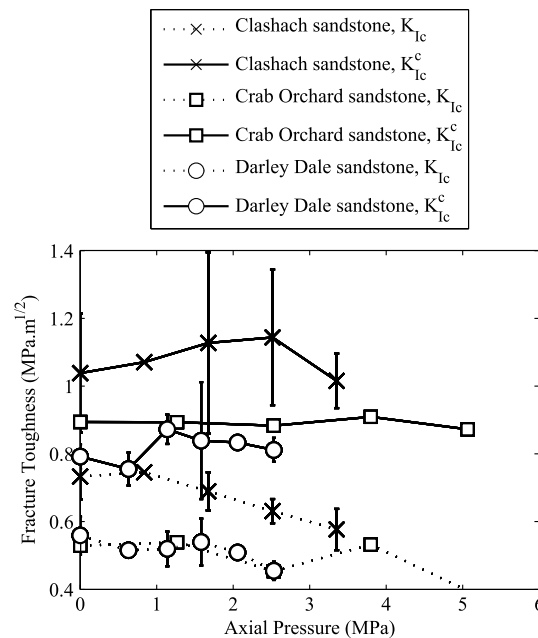


**Figure A1.** Measured  $K_{Ic}$  and  $K_{Ic}^c$  as a function of applied axial pressure for three sandstone materials.

described in section 3. Figure A1 shows the apparent fracture toughnesses,  $K_{Ic}$  and  $K_{Ic}^c$ , as a function of the applied axial pressure for Clashach, Crab Orchard, and Darley Dale sandstones. Apparent fracture toughness was observed to decrease slightly over the low axial pressure range tested, in agreement with the effect observed by *Ingraffea et al.* [1984]. However,  $K_{Ic}$  decreases at a greater rate than for the granite and limestone measured by *Ingraffea et al.* [1984]. Applying the ductility correction leads to a much smaller decrease in  $K_{Ic}^c$  than in  $K_{Ic}$ .

*Ingraffea et al.* [1984] suggest that the decrease in measured  $K_{Ic}$  with applied axial pressure occurs for the Indiana limestone because the applied pressure is not insignificant relative to the compressive strength of the rock. The axial pressure required to successfully propagate fractures through the Mancos shale in the Arrester orientation is equivalent to 1.5% of the compressive strength found in Table 1, so from the relations observed in the Darley Dale, Clashach, and Crab Orchard sandstones it was deemed likely that the axial pressure does not affect  $K_{Ic}^c$ .

Figure A1 does not show a fall in apparent  $K_{Ic}$  of more than 5% with  $1.5\%\sigma_c$  applied as an axial pressure. This is lower than the observed variation in Arrester orientation  $K_{Ic}$  measurements in the Mancos shale, so the axial pressure effect was also deemed negligible on  $K_{Ic}$ .

#### Acknowledgments

This work was supported by ExxonMobil URC and a UCL Impact award. NB acknowledges support from the Natural Environment Research Council (grant NE/K009656/1). The authors are also grateful to Jacky Kendrick, Fiona King, Helen Lacey, and Jabraan Ahmed for their work on various aspects of this paper. Thanks finally to Neil Hughes, John Bowles, Steve Boon, and Jim Davy for their work on developing the experimental methodology used here. The data used are listed in the tables and references within this document.

#### References

- Abou-Sayed, A. (1977), Fracture toughness of triaxially loaded Indiana limestone, paper presented at 18th U.S. Symposium on Rock Mechanics, Energy Resources and Excavation Technology.
- American Society for Testing and Materials (2002), *D2938-95 Standard Test Method for Unconfined Compressive Strength of Intact Rock Core Specimens*, *ASTM Book of Standards*, Am. Soc. for Test. and Mater., West Conshohocken, Pa.
- Barker, L. (1979), Theory for determining  $K_{Ic}$  from small, non-LEFM specimen, supported by experiments on aluminium, *Int. J. Fract.*, *15*, 515–536.
- Barker, L., and R. Guest (1978), Compliance calibration of the short rod fracture toughness specimen, *Rep. TR-78-20*, Terra Tek, Salt Lake City, Utah.
- Bartsch, M., Z. Zhang, C. Scheu, M. Ruhle, and U. Messerschmidt (2004), Fracture parameters of chevron-notched  $Al_2O_3/Nb$  sandwich specimens, *Int. J. Mater. Res.*, *95*(9), 779–784.
- Benson, P. M., P. G. Meredith, and E. S. Platzman (2003), Relating pore fabric geometry to acoustic and permeability anisotropy in crab orchard sandstone: A laboratory study using magnetic ferrofluid, *Geophys. Res. Lett.*, *30*(19), 1976, doi:10.1029/2003GL017929.
- Berryman, J. (2008), Exact seismic velocities for transversely isotropic media and extended thomsen formulas for stronger anisotropies, *Geophysics*, *73*(1), D1–D10, doi:10.1190/1.2813433.
- Burns, C. (2011), Shale gas—A global overview, in *Shale Gas: Challenging the Frontiers of E and P*, Soc. of Pet. Eng., London.
- Chidsey, T., and C. Morgan (2010), Utah Shale Gas Activity Update 2010, paper presented at EMD Annual Leadership Meeting—Gas Shale Committee Report, Energy Minerals Division, AAPG, Tulsa.
- Chong, K. P., M. D. Kuruppu, and J. S. Kuszmaul (1987), Fracture toughness determination of layered materials, *Eng. Fract. Mech.*, *28*(1), 43–54, doi:10.1016/0013-7944(87)90118-4.

- Costin, L. (1981), *Static and Dynamic Fracture Behaviour of Oil Shale*, pp. 169–184, ASTM Spec. Tech. Publ., Philadelphia, Pa.
- Cotterell, B., and J. Rice (1980), Slightly curved or kinked cracks, *Int. J. Fract.*, *16*(2), 155–169, doi:10.1007/BF00012619.
- Crawford, B., B. Smart, I. Main, and F. Liakopoulou-Morris (1995), Strength characteristics and shear acoustic anisotropy of rock core subjected to true triaxial compression, *Int. J. Rock Mech. Min. Sci. Geomech. Abstr.*, *32*(3), 189–200, doi:10.1016/0148-9062(94)00051-4.
- Cui, Z.-D., D.-A. Liu, G.-M. An, B. Sun, M. Zhou, and F.-Q. Cao (2010), Technical note, *Int. J. Rock Mech. Min. Sci.*, *47*(5), 871–876, doi:10.1016/j.ijrmms.2009.12.015.
- Eseme, E., J. Urai, B. Krooss, and R. Littke (2007), Review of mechanical properties of oil shales: Implications for exploitation and basin modelling, in *Oil Shale*, edited by E. Reinsalu, pp. 159–174, Estonian Acad., Tallinn, Estonia.
- Grant, T., L. Weber, and A. Mortensen (2000), Plasticity in chevron-notch fracture toughness testing, *Eng. Fract. Mech.*, *67*(3), 263–276, doi:10.1016/S0013-7944(00)00061-8.
- Hanson, J., and A. Ingraffea (1997), Standards for fracture toughness testing of rock and manufactured ceramics: What can we learn for Concrete, *Cem. Concr. Aggr.*, *19*(2), 103–111.
- Homand, F., T. Belem, and M. Souley (2001), Friction and degradation of rock joint surfaces under shear loads, *Int. J. Numer. Anal. Methods Geomech.*, *25*(10), 973–999, doi:10.1002/nag.163.
- Hutchinson, J. W., and Z. Suo (1992), Mixed mode cracking in layered materials, *Adv. Appl. Mech.*, *29*, 63–191.
- Ingraffea, A., K. Gunsallus, J. Beech, and P. Nelson (1984), A short-rod based system for fracture toughness testing of rock, in *Chevron-Notched Specimens: Testing and Stress Analysis, ASTM STP 855*, edited by J. Underwood, S. Freiman, and F. Baratta, pp. 152–166, Am. Soc. for Test. and Mater., Philadelphia, Pa.
- International Society of Rock Mechanics (ISRM) (1978), Suggested methods for determining tensile strength of rock materials, *Int. J. Rock Mech. Min. Sci. Geomech. Abstr.*, *15*, 99–103.
- International Society of Rock Mechanics (ISRM) (1988), Suggested Methods for determining the fracture toughness of rock, *Int. J. Rock Mech. Min. Sci. Geomech. Abstr.*, *25*, 71–96.
- Kennedy, A. (2011), Geologic Predictors of the hydrocarbon extraction potential of the Mancos Shale, PhD thesis, Univ. of Utah, Utah.
- Khazan, Y. M., and Y. A. Fialko (1995), Fracture criteria at the tip of fluid-driven cracks in the earth, *Geophys. Res. Lett.*, *22*(18), 2541–2544, doi:10.1029/95GL02547.
- King, F. (2013), An investigation into the porosity of the Mancos Shale, UCL Master's thesis, Univ. College London, London.
- Krishnan, G., X. Zhao, M. Zaman, and J.-C. Roegiers (1998), Fracture toughness of a soft sandstone, *Int. J. Rock Mech. Min. Sci.*, *35*(6), 695–710, doi:10.1016/S0148-9062(97)00324-0.
- Lawn, B. (1993), *Fracture of Brittle Solids*, 2nd ed., Cambridge Univ. Press, Cambridge, U. K.
- Lee, H. P., J. E. Olson, J. Holder, J. F. W. Gale, and R. D. Myers (2015), The interaction of propagating opening mode fractures with preexisting discontinuities in shale, *J. Geophys. Res. Solid Earth*, *120*, 169–181, doi:10.1002/2014JB011358.
- Lim, I., I. Johnston, S. Choi, and J. Boland (1994), Fracture testing of a soft rock with semi-circular specimens under three-point bending. Part 1 mode I, *Int. J. Rock Mech. Min. Sci. Geomech. Abstr.*, *31*(3), 185–197, doi:10.1016/0148-9062(94)90463-4.
- Longman, M., and R. Koepsell (2005), *Defining and Characterizing Mesaverde and Mancos Sandstone Reservoirs Based on Interpretation of Formation Microimager (FMI) Logs*, Utah Geol. Surv., Eastern Uinta Basin, Utah.
- Loucks, R., R. Reed, S. Ruppel, and D. Jarvie (2012), Morphology, genesis, and distribution of nanometer-scale pores in siliceous mudstones of the mississippian barnett shale, *J. Sediment. Res.*, *79*, 848–861.
- McLennan, J., J. Roegiers, and W. Marx (1983), The mancos formation: An evaluation of the interaction of geological conditions, treatment characteristics and production, in *Low Permeability Gas Reservoirs Symposium*, edited by R. M. McLennan, pp. 63–69, SPE/DOE, Denver, Colo.
- Meredith, P. G. (1989), Comparative fracture toughness testing of rocks, in *Fracture Toughness and Fracture Energy: Test Methods for Concrete and Rock*, edited by H. Mihashi, H. Takahashi, and F. H. Wittman, pp. 265–278, Brookfield, Rotterdam.
- Migliazza, M., A. M. Ferrero, and A. Spagnoli (2011), Experimental investigation on crack propagation in carrara marble subjected to cyclic loads, *Int. J. Rock Mech. Min. Sci.*, *48*(6), 1038–1044, doi:10.1016/j.ijrmms.2011.06.016.
- Nadeau, P., and R. Reynolds (1981), Burial and contact metamorphism in the Mancos Shale, *Clays Clay Miner.*, *29*, 249–259.
- Nuismer, R. (1975), An energy release rate criterion for mixed mode fracture, *Int. J. Fract.*, *11*(2), 245–250, doi:10.1007/BF00038891.
- Ouchterlony, F. (1989), On the background to the formulae and accuracy of rock fracture toughness measurements using {ISRM} standard core specimens, *Int. J. Rock Mech. Min. Sci. Geomech. Abstr.*, *26*(1), 13–23, doi:10.1016/0148-9062(89)90521-4.
- Paterson, M., and T. Wong (2005), *Experimental Rock Deformation—The Brittle Field, Minerals and Rocks*, Springer, Berlin.
- Pyrak-Nolte, L. J., L. R. Myer, and N. G. W. Cook (1990), Anisotropy in seismic velocities and amplitudes from multiple parallel fractures, *J. Geophys. Res.*, *95*(B7), 11,345–11,358, doi:10.1029/JB095iB07p11345.
- Rist, M. A., P. R. Sammonds, H. Oerter, and C. S. M. Doake (2002), Fracture of antarctic shelf ice, *J. Geophys. Res.*, *107*(B1), 2002, doi:10.1029/2000JB000058.
- Sarker, R., and M. Batzle (2010), Anisotropic elastic moduli of the Mancos B Shale—An Experimental Study, paper presented at 2010 SEG Annual Meeting, Denver, Colo., 17–22 Oct.
- Schamel, S. (2005), *Shale Gas Reservoirs of Utah: Survey of an Unexploited Potential Energy Resource*, Utah Geol. Surv. Salt Lake City, Utah.
- Schmidt, R., and C. Huddle (1977a), *Fracture Mechanics of Oil Shale—Some Preliminary Results*, Sandia Labs., Albuquerque, N. M.
- Schmidt, R., and C. Huddle (1977b), Effect of confining pressure on fracture toughness of indiana limestone, *Int. J. Rock Mech. Min. Sci. Geomech. Abstr.*, *14*(5–6), 289–293, doi:10.1016/0148-9062(77)90740-9.
- Sone, H., and M. D. Zoback (2013), Mechanical properties of shale-gas reservoir rocks—Part 1: Static and dynamic elastic properties and anisotropy, *Geophysics*, *78*(5), D381–D392, doi:10.1190/geo2013-0050.1.
- Suo, Z., G. Bao, B. Fan, and T. Wang (1991), Orthotropy rescaling and implications for fracture in composites, *Int. J. Solids Struct.*, *28*(2), 235–248.
- Terratek (2008), Deeptrak phase 1 and 2—Improving deep drilling performance—An industry/DOE program to develop and benchmark advanced diamond product drill bits and HP/HT drilling fluids to significantly improve rates of penetration, *U.S. Dept. of Energy - DE-FC26-02NT41657*, Terratek, Salt Lake City, Utah.
- Thiercelin, M., R. Jeffrey, and K. B. Naceur (1989), Influence of fracture toughness on the geometry of hydraulic fractures, SPE-16431-PA presented at SPE Production Engineering, pp. 435–442, Soc. of Petrol. Eng.
- Thomsen, L. (1986), Weak elastic anisotropy, *Geophysics*, *51*(10), 1954–1966, doi:10.1190/1.1442051.
- Tsvankin, I. (2001), *Seismic Signatures and Analysis of Reflection Data in Anisotropic Media*, Pergamon, New York.
- Vanickobchinda, P., D. Reddish, L. Stace, and D. Whittles (2007), Numerical simulation of the dynamic breakage testing of sandstone. Part I: Development of homogeneous constitutive model for the fragmentation analysis in sandstone, *Int. J. Mater. Struct. Reliab.*, *5*, 29–44.

- Wang, C., and R. Pilliar (1989), Short-rod elastic-plastic fracture toughness test using miniature specimens, *J. Mater. Sci.*, *24*(7), 2391–400, doi:10.1007/BF01174501.
- Wang, Z. (2002a), Seismic anisotropy in sedimentary rocks, Part 2: Laboratory data, *Geophysics*, *67*(5), 1423–1440.
- Wang, Z. (2002b), Seismic anisotropy in sedimentary rocks, Part 1: A single-plug laboratory method, *Geophysics*, *67*(5), 1415–1422.
- Warpinski, N., and M. Smith (1990), Rock mechanics and fracture geometry, in *Recent Advances in Hydraulic Fracturing*, edited by J. Gidley et al., pp. 57–80, Soc. of Petrol. Eng., Texas.
- Weinberger, R., Z. Reches, and A. Eidelman (1994), Tensile properties of rocks in four-point beam tests under confining pressure, in *Rock Mechanics*, edited by P. Nelson and S. E. Laubach, pp. 435–442, Balkema, Rotterdam.
- Wong, L., C. Zou, and Y. Cheng (2014), Fracturing and failure behavior of carrara marble in quasistatic and dynamic Brazilian disc tests, *Rock Mech. Rock Eng.*, *47*(4), 1117–1133, doi:10.1007/s00603-013-0465-9.
- Young, C., N. Patti, and B. Trent (1982), Stratigraphic variations in oil-shale fracture properties, *US DOE Rep. of Invest.*, *DOE/LC/RI-82-5*, Dept. of Energy, Laramie, Wyoming.
- Zhang, Z. (2002), An empirical relation between mode I fracture toughness and the tensile strength of rock, *Int. J. Rock Mech. Min. Sci.*, *39*(3), 401–406.